Long-Term Offshore Borehole Fluid-Pressure Monitoring at the Northern Cascadia Subduction Zone and Inferences Regarding the State of Megathrust Locking

Earl E. Davis, Tianhaozhe Sun, Martin Heesemann, Keir Becker, Angela Schlesinger

June 2023

Geochemistry, Geophysics, Geosystems®

AGU ADVANCING EARTH AND SPACE SCIENCE

RESEARCH ARTICLE
10.1029/2023GC010910

Key Points:

- 8-year formation pressure records from northern Cascadia suggest a lack of tectonic transients despite occasional large dynamic stressing
- Noise level of the record defines a detection threshold of 0.08 kPa, equivalent to 16 nanostrain for shallow accretionary prism sediment
- Deformation modeling shows that the data would resolve local slip down to <1 cm, and thus suggests a fully locked state of the megathrust

Correspondence to:
E. E. Davis and T. Sun,
earldavis@shaw.ca;
tianhaozhe.sun@nrcan-rncan.gc.ca

Citation:
Davis, E. E., Sun, T., Heesemann, M., Becker, K., & Schlesinger, A. (2023). Long-term offshore borehole fluid-pressure monitoring at the northern Cascadia subduction zone and inferences regarding the state of megathrust locking. *Geochemistry, Geophysics, Geosystems*, *24*, e2023GC010910. https://doi.org/10.1029/2023GC010910

Received 14 FEB 2023
Accepted 7 MAY 2023

Author Contributions:
Conceptualization: Earl E. Davis, Tianhaozhe Sun
Data curation: Martin Heesemann, Angela Schlesinger
Formal analysis: Earl E. Davis, Tianhaozhe Sun, Keir Becker
Funding acquisition: Earl E. Davis, Martin Heesemann, Keir Becker
Investigation: Tianhaozhe Sun
Methodology: Tianhaozhe Sun
Resources: Earl E. Davis, Martin Heesemann, Keir Becker

Long-Term Offshore Borehole Fluid-Pressure Monitoring at the Northern Cascadia Subduction Zone and Inferences Regarding the State of Megathrust Locking

Earl E. Davis[1], Tianhaozhe Sun[1], Martin Heesemann[2], Keir Becker[3], and Angela Schlesinger[2]

[1]Pacific Geoscience Centre, Geological Survey of Canada, Sidney, BC, Canada, [2]Ocean Networks Canada, University of Victoria, Victoria, BC, Canada, [3]Rosenstiel School of Marine, Atmospheric and Earth Science, University of Miami, Miami, FL, USA

Abstract The Cascadia subduction megathrust off the Pacific Northwest follows an "end member" seismogenic behavior, producing large (up to moment magnitude 9) but infrequent (every several hundred years) earthquakes and tsunamis. Crustal deformation associated with the ongoing plate convergence has been characterized by land-based geodetic observations, but the state of locking across the full breadth of the seismogenic fault is poorly constrained. We report results of offshore monitoring of borehole fluid pressure, as a proxy for formation volumetric strain, at a site ~20 km landward of the Cascadia subduction deformation front since 2010. The multi-depth pressure records were plagued by hydrologic noise, but noise at the deepest monitoring level (303 m sub-seafloor) abated in 2015. Subsequently, including at the times of regional large earthquakes that caused significant dynamic stressing, no persistent pressure transients are present above a threshold of 0.08 kPa imposed by unremovable oceanographic signals, corresponding to a strain detection limit of ~16 nanostrain. Simple dislocation models using local megathrust geometry suggest a resolvable slip of <1 cm along a trench-normal corridor beneath the borehole for a range of slip-patch dimensions. A large slip patch can be well resolved even at considerable along-strike distances from the borehole; for instance, ~10 cm slip is detectable over a 200-km strike range for a slip-patch radius of ~50 km. This high sensitivity for detecting slip, along with the lack of observed events, stands in stark contrast to observations at other subduction zones, and suggests that the Northern Cascadia megathrust is most likely fully locked.

Plain Language Summary Subduction thrust faults can produce Earth's largest earthquakes and tsunamis. Estimating the seismic and tsunami potential requires knowing how complete the fault locking is. The Cascadia subduction zone is known to have hosted very large earthquakes, but with the existing measurements of deformation being on land, the state of locking of the shallow sub-marine portion of the fault remains unclear. Addressing this question requires offshore deformation measurements directly above the shallow fault. In this study, we report results of formation fluid pressure measurement—as a volumetric strain indicator—from a deep-ocean borehole off Vancouver Island near the deformation front of Cascadia. While data from shallow monitoring depths suffer from noise likely caused by formation gas dynamics, the record from the deepest level (300 m beneath the seafloor) has been sufficiently quiet since mid-2015 to allow detection of any slip-triggered pressure variations. Lack of such variations, together with deformation modeling, limits local slip events to be <1 cm. This suggests that the slip deficit of the plate convergence is being accumulated at a substantial rate and it may be released in the next megathrust earthquake. This contrasts with other subduction margins where slip-related pressure transients have been frequently detected.

1. Introduction

The generation of subduction megathrust earthquakes requires the plate-interface fault to be locked or partially locked between earthquakes, causing accumulation of slip deficit and elastic strain to be released in future ruptures. Determining the locking state of the megathrust, in particular at its offshore near-trench portion, thus remains crucial for seismic and tsunami hazard assessment. Traditional onshore geodetic measurements (e.g., Global Navigation Satellite System—GNSS) are generally insensitive to the near-trench slip deficit (e.g., K. Wang & Tréhu, 2016), and sub-marine geodetic observations are critical for determining the locking state and slip behavior of the shallow subduction megathrust. This is made clear by the range of slip deficit allowed by models

Visualization: Earl E. Davis, Tianhaozhe Sun
Writing – original draft: Earl E. Davis, Tianhaozhe Sun
Writing – review & editing: Earl E. Davis, Tianhaozhe Sun, Martin Heesemann, Keir Becker, Angela Schlesinger

that are kinematically constrained by onshore observations alone (Li et al., 2018; Schmalzle et al., 2014) (cf. Figures 1a and 1b). Examples of offshore geodesy from multiple subduction margins (Araki et al., 2017; Davis et al., 2013, 2015; Ito et al., 2013; Kido et al., 2011; Sato et al., 2011; Sun et al., 2014; Sun, Davis, et al., 2017; Sun, Wang, et al., 2017; Tomita et al., 2017; Wallace, Araki, et al., 2016; Wallace, Webb, et al., 2016; Watanabe et al., 2014; Yokota et al., 2016; see also Bürgmann & Chadwell, 2014, and references therein) have documented various modes of slip over the broad seismic-to-aseismic spectrum (e.g., Bürgmann, 2018; Ide et al., 2007; Obara & Kato, 2016; Saffer & Wallace, 2015). In this work, we report offshore geodetic evidence for the state of locking of the northern Cascadia subduction fault, based on long-term (decadal) monitoring of borehole fluid pressure in the frontal accretionary prism above the shallow megathrust.

Studying the present-day locking state of the Cascadia megathrust and estimating the sizes of future earthquakes and tsunamis have great societal importance to the west coast of North America. Continuously advancing observations and modeling studies have led to remarkable progress in understanding the Cascadia megathrust and the processes of great subduction earthquakes (Walton et al., 2021; K. Wang & Tréhu, 2016). These observational and modeling advances include long-term seismological and geodetic monitoring (e.g., Bartlow, 2020; Dragert et al., 2001; McCaffrey et al., 2013; McCrory et al., 2012; Rogers & Dragert, 2003; Stone et al., 2018; Toomey et al., 2014), lithospheric scale geophysical imaging (e.g., Audet & Schaeffer, 2018; Carbotte et al., 2022; Davis & Hyndman, 1989; Han et al., 2017; Nedimović et al., 2003; Yuan et al., 1994), paleo-seismology and -tsunami studies of historical ruptures (e.g., Atwater et al., 1995; Goldfinger et al., 2012; Priest et al., 2010; P. L. Wang et al., 2013), laboratory studies of fault-rock frictional properties (e.g., Ikari et al., 2009; Stanislowski et al., 2022), and modeling of the seismogenic extent constrained by thermal and/or deformation observations (e.g., Hyndman & Wang, 1993; Melgar et al., 2022; Schmalzle et al., 2014; K. Wang et al., 2003). Nonetheless, existing models of the Cascadia megathrust locking distribution are all constrained solely by land-based GNSS measurements (Li et al., 2018; Pollitz & Evans, 2017; Schmalzle et al., 2014; K. Wang et al., 2003). These measurements reveal episodic slip downdip of the locked portion of the subduction plate interface in considerable spatial and temporal detail (Bartlow, 2020; Dragert et al., 2001, 2004; Saux et al., 2022) but leave large uncertainties in determining the offshore locking state (K. Wang & Tréhu, 2016) (Figures 1a and 1b). Direct sub-marine geodetic constraints are thus urgently needed.

Here we present formation fluid pressure observations recorded in the IODP (Integrated Ocean Drilling Program) Hole U1364A, where an ACORK (Advanced Circulation Obviation Retrofit Kit) observatory was installed on 29 July 2010, during IODP Expedition 328 off Vancouver Island (Davis et al., 2010; see Section 2) (Figures 1b–1d). With the low permeability of the subduction prism sediments, fluid pressure monitored in the sealed borehole serves as an effective proxy for the volumetric strain of the surrounding formation at the timescales of typical slow slip events (SSE) (less than months) or shorter. While similar observation systems installed at Nankai (Araki et al., 2017; Davis et al., 2013), Costa Rica (Davis et al., 2015; Sun, Davis, et al., 2017), and Hikurangi (Wallace et al., 2021) have unambiguously detected transient signals due to local slip along those subduction megathrusts, our investigation of the 12-year Cascadia records suggests an absence of pressure transients associated with regional tectonic events (see Section 4). Analysis of the pressure data's detection threshold, together with simple dislocation modeling (see Sections 5), suggests very high sensitivity for resolving offshore slip along the megathrust and indicates complete or near-complete fault locking over an extent of 100–200 km in the strike direction off Vancouver Island.

2. Observational Methods

2.1. History of Drilling at Northern Cascadia

IODP Hole U1364A was drilled into the outer Cascadia subduction zone accretionary prism off Vancouver Island, Canada (Figure 1), where much of the thick section of turbidite and hemipelagic sediments deposited on the eastern flank of the Juan de Fuca Ridge has been scraped off the under-thrusting oceanic crust (Davis & Hyndman, 1989; Han et al., 2016; Hyndman et al., 1990; Westbrook et al., 1994). The sediments that bury the incoming igneous oceanic crust are locally about 2.7 km thick at the trench; at the drilling site, roughly 20 km landward of the deformation front (Figure 1c), the accreted sedimentary section is nearly doubled to a thickness of approximately 5 km (Yuan et al., 1994). During this tectonic thickening and the accompanied sediment compaction, pore fluids are expelled, and gas (primarily biogenic methane) is transported upward to contribute to the formation of solid gas hydrates within the zone of hydrate stability a few hundred meters beneath the

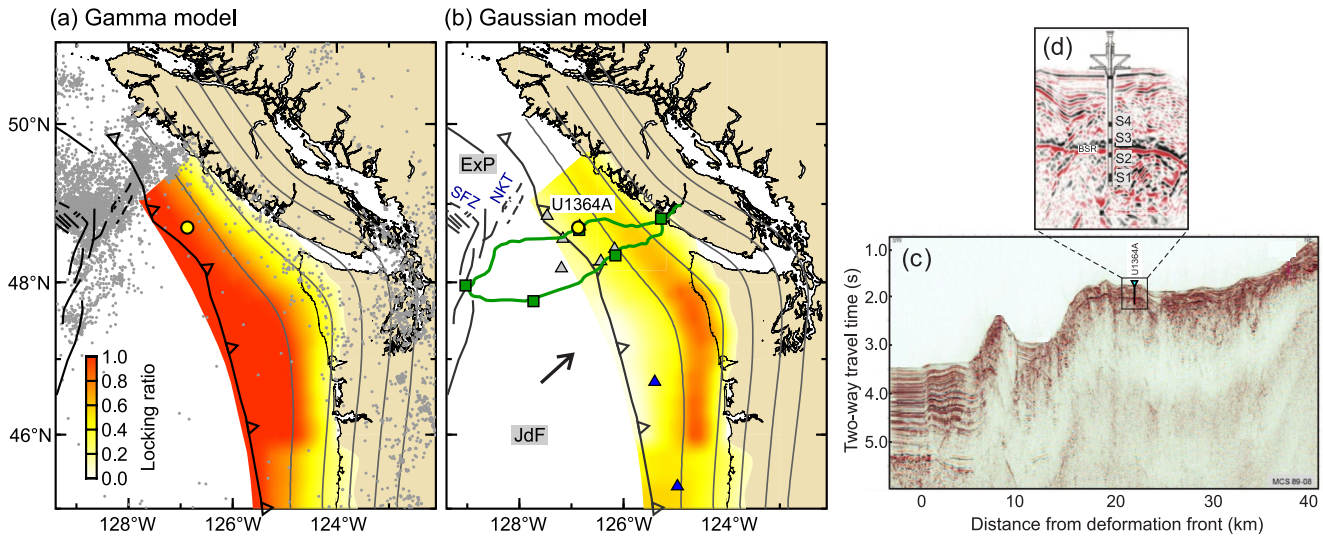

Figure 1. Maps, Hole U1364A location, and borehole observatory configuration. (a, b) Location of Hole U1364A (yellow-filled circle), in the context of the range of Cascadia subduction fault locking distribution estimated by Schmalzle et al. (2014) using terrestrial Global Navigation Satellite System (GNSS) observations. Also shown are plate-interface depth at 10-km contour interval (gray lines; McCrory et al., 2004), seismicity since 2000 (gray dots in panel a; International Seismological Centre, 2022), Ocean Networks Canada NEPTUNE observatory cable and nodes (green line and squares in b), existing seafloor GNSS-Acoustic site locations (gray triangles: Canadian sites; blue triangles: US sites; DeSanto et al., 2022; Hutchinson & Heesemann, 2022), and the relative plate motion of c. 42 mm yr^{-1} between Juan de Fuca and North America Plates (black arrow in b). JdF: Juan de Fuca Plate, ExP: Explorer Plate, SFZ: Sovanco Fracture Zone, NKT: Nootka Fault Zone. (c) Hole U1364A location shown in the context of a seismic reflection profile crossing the frontal Cascadia accretionary prism. (d) Observatory configuration, with screen positions shown relative to the local bottom-simulating reflector (BSR) that identifies the methane gas-hydrate/gas boundary. Seaward of the deformation front, sediment thickness is roughly 2.5 km. The depth of the BSR at U1364A is ~230 m.

seafloor, accumulation of free gas in the pore volume beneath that, and a bottom simulating seismic reflection from the gas-hydrate/free-gas boundary (Davis et al., 1990; Haacke et al., 2007; Hyndman & Davis, 1992; Riedel et al., 2010) (Figures 1c and 1d).

The area near Hole U1364A was visited previously during ODP (Ocean Drilling Program) Leg 146 and IODP Expedition 311 in 1992 and 2005, respectively (Riedel et al., 2006; Westbrook et al., 1994), in part to study the processes of gas hydrate formation. Data from coring and logging provided extensive information regarding the sediment lithology and physical properties, and an attempt was made during the first of these drilling expeditions to establish a borehole observatory for formation-fluid sampling and pressure and temperature monitoring (Westbrook et al., 1994). In that early attempt, sediment intruded into the interior of the hole casing, causing the thermistor string and fluid sampling line to interfere with the CORK/casing seal. The unfortunate experience paved the way to later developments of borehole completion schemes better suited to unconsolidated and semi-consolidated sediment sections, including the ACORK configuration used for Hole U1364A (Davis & Heesemann, 2012; Davis et al., 2010). Completed in 2010, this hole was drilled without coring or logging, with the sole intent of establishing an ACORK observatory for pressure, temperature, seismic, and tilt monitoring (Becker et al., 2020; Davis & Heesemann, 2012; McGuire et al., 2018), with instrument connections to shore for power and data telemetry (Heesemann et al., 2014).

2.2. Hole U1364A Observatory Configuration

Hole U1364A was drilled to a total depth of 336 m below the seafloor (mbsf) through roughly 90 m of gently deformed slope-basin deposits and underlying consolidated sediments of the accretionary prism that are folded and faulted on a scale too small to be resolved in seismic reflection profiles. The configuration of the ACORK observatory, installed immediately after drilling, is shown schematically in Figure 1d. The observatory was constructed with solid 10.75-inch o.d. casing, left open at the wellhead above the seafloor, but sealed at the bottom of the casing with a bridge plug backed with cement (Davis & Heesemann, 2012). This left the casing interior open to a depth of 302 mbsf for instruments requiring thermal or mechanical (but not direct) contact with the formation, specifically a seismometer, tilt meter, and thermistor cable deployed in 2016 and connected to the Ocean Networks Canada (ONC) NEPTUNE cable in 2017, as described in Section 2.3.

Formation fluid pressures are transmitted to sensors (Paroscientific Digiquartz model 8B4000, 40 mPa full scale) at the wellhead via 2.03-m-long circumferential sand-packed filter screens and 3-mm-diameter (1/8-inch) i.d. stainless-steel hydraulic tubing mounted on the outside of the casing. Screens (numbered S1–S4 from bottom to top) are positioned at depths of 304, 244, 203, and 156 mbsf. The middle two pressure monitoring screens were positioned 14 m below and 27 m above the base of the gas hydrate stability zone at 230 mbsf to detect any effects of free gas and gas hydrate in the sediment matrix by way of tidal loading efficiency differences, or diffusive signals originating at the hydrate-gas boundary (e.g., K. Wang et al., 1998). The lowermost and uppermost screens were placed 74 m below and above the boundary, distances that were anticipated to be sufficient to avoid hydrologic complications originating at the boundary. Pressure monitoring began under battery power prior to installation on 29 July 2010, with a sampling rate of once per minute. All sensors were interrogated simultaneously (within milliseconds), allowing accurate comparisons to be made among records from all monitoring depths at all frequencies up to those limited by the sampling rate. Upon connecting to the NEPTUNE cable on 12 June 2017, onboard power and memory constraints were lifted, and the sampling rate was increased to once per second. Early data downloaded on 12 July 2011, indicated that a seafloor-reference pressure sensor, also mounted on the wellhead, had failed earlier that year (21 February), causing all logging to cease. During the course of this ROV program, the problem was diagnosed, and on 24 July 2011, the cable to the seafloor sensor was cut, logging was restored, and the hydraulic input to the sensor originally assigned to the uppermost screen (S4) was switched to monitor seafloor pressure.

2.3. Complementary Seismic and Temperature Instrumentation

In addition to the ACORK pressure records, complementary seismic data have been acquired for the full history of ACORK operations by buried seismometers and accelerometers at the ONC Clayoquot Slope node (site NC89), roughly 3.5 km along strike from Hole U1364A, and for an 11-month period (June 2017 to May 2018) from the seismometer that was clamped within the ACORK casing at 280 mbsf (CQS64; McGuire et al., 2018). Temperatures were monitored over a nearly 2-year period (July 2016–May 2018) with a thermistor cable spanning from the seafloor to the seismometer/tilt meter unit (Becker et al., 2020). Other instruments providing regional geophysical data via the NEPTUNE cable system include buried seismometers and accelerometers, bottom pressure recorders, and CORK borehole observatories on the Juan de Fuca Ridge and eastern ridge flank (at locations shown in Figure 1b). More instrument details can be found at the ONC website (https://www.oceannetworks.ca), and seismic and pressure data are accessible through the Incorporated Research Institutions for Seismology (IRIS) Data management center (http://ds.iris.edu/wilber3/find_event) and ONC data portal website (https://data.oceannetworks.ca/DataSearch), respectively.

Relationships among collocated ground motion, seafloor pressure, and formation fluid pressure measurements have proven useful for studying dynamic ocean-crust coupling (Sun & Davis, 2022) and for characterizing the mechanical properties of the oceanic crust and the outer accretionary prism and their response to seismic and oceanographic loading (e.g., Davis & Farrugia, 2021; Sun et al., 2021). In an examination of the Hole U1364A 11-month borehole seismometer, tilt meter, and fluid pressure data, McGuire et al. (2018) found no indications of deformation during that monitoring period. Similarly, temperature data recorded by the borehole thermistors over the period of its operation showed no signs of hydrologic activity that might be associated with tectonic events (Becker et al., 2020). In this study, we report an interpretation based on the full history of U1364A borehole pressure that now spans 12.5 years.

3. Results: Description of Borehole Pressure Data

3.1. Raw Data

The full history of pressure recording at Hole U1364A is shown in Figure 2. Notable characteristics include: (a) high levels of variability at all screens in the first 5 months of monitoring, with progressively greater amplitudes from deeper to shallower levels (S1–S3); (b) diminishing variations after mid-2011, with the largest amplitudes typically seen at S2 prior to mid-2014; (c) a continued reduction in the amplitudes and frequency of occurrence of pressure excursions at S1 and S2 until they largely abated in early 2015; (d) erratic variations at S3 persisting to the present; (e) tidal frequency signals of varying amplitudes relative to seafloor pressure; (f) relatively stable average pressures at S3 from mid-2015 to the present; (g) a rising trend of pressure at S1 since early 2013, rising

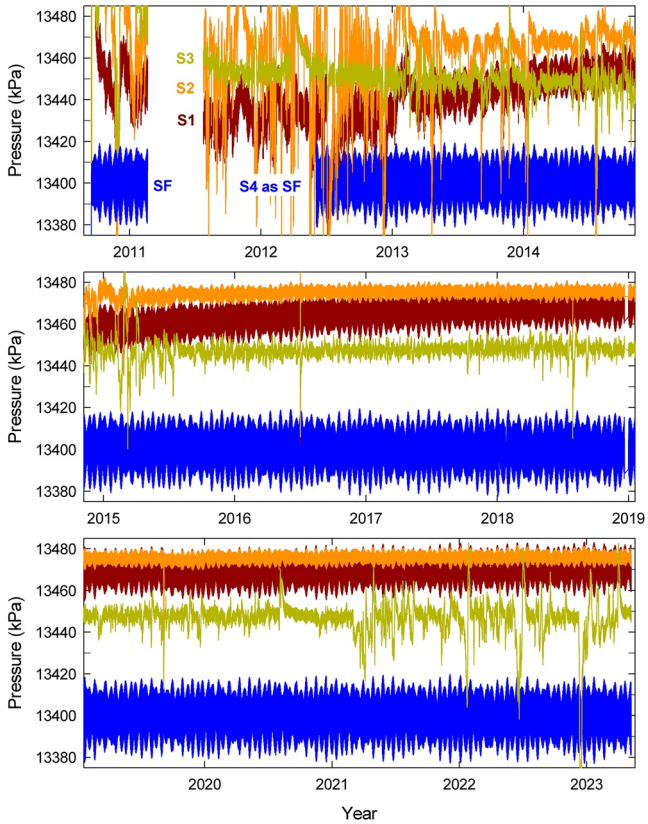

Figure 2. Raw pressure data spanning the full recording period at Hole U1364A to date, with offsets applied that account for thermal effects of a sampling rate change in 2017, and the in situ inter-sensor calibration in 2019 (see Section 3.2). Pressure records are color coded according to the sensor levels, as indicated in the top panel.

toward the pressure at S2; and (h) present average pressures of roughly 70, 75, and 47 kPa relative to hydrostatic at S1, S2, and S3 (a small fraction of the lithostatic state at all these depths). In the sub-sections that follow, we discuss steps to improve the resolution of the pressure observations, understand and reduce levels of noise, and improve the ability to detect signals caused by possible slip on the underlying subduction megathrust.

3.2. Pressure Sensor Temperature Compensation and In Situ Calibrations

A first step in processing data is to remove the effects of temperature sensitivity of the pressure sensors in the presence of bottom-water temperature variations. Compensation is often done with calibrations carried out by the manufacturer using the temperature-sensitive output of an internal unloaded quartz crystal. At Hole U1364A, only the seafloor sensor had a temperature-sensing crystal; other sensors were provided by Paroscientific with temperature-compensation parameters based on externally measured temperature. Because the seafloor sensor failed in 2011, temperatures monitored by an onboard platinum thermometer were employed for tracking bottom-water temperature, and these data were used to compensate for the temperature sensitivity of each sensor using the factory-determined compensation coefficients. Accuracy is limited by the contrasting thermal time constants of the platinum thermometer (mounted to the steel instrument pressure case with thermal contact grease) and pressure sensors (with thermally resistant shock mounts), but this yields no impact on signals having periods longer than a few minutes. The magnitude of the temperature sensitivity of the raw pressure values and the effectiveness of its removal are illustrated in Figure 3.

In addition to the effects of natural temperature variations, small effects were seen when the sampling rate changed from 1/min to 1/s at the time of connection to ONC's NEPTUNE cable (12 July 2017). This is thought to be a result of sensor self-heating, and the observed offsets (−1.4, −1.8, −1.5, and −1.7 kPa for sensors connected to S1, S2, S3, and the seafloor, respectively) have been used to correct (with offsets of opposite sign) all data recorded during the early lower-sampling-rate battery-powered operations.

An additional step in processing the pressure data is to determine and correct for offsets that are the consequence of the unavoidable limits to the precision of laboratory calibrations (done at the time of manufacture by

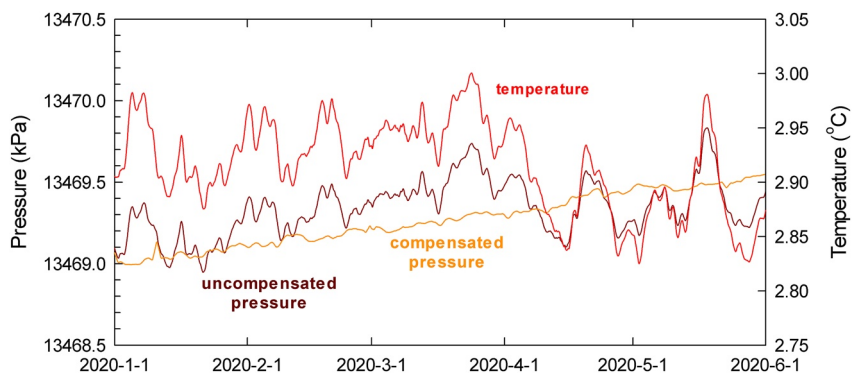

Figure 3. Illustration of a pressure sensor's temperature sensitivity and the corresponding data correction for temperature compensation. Bottom-water temperatures measured using the CORK onboard platinum thermometer are shown in red, uncorrected values of the S1 pressure sensor are shown in dark red, and temperature-compensated pressures, computed with factory-determined parameters, are shown in orange. A 1-hr moving average has been applied to reduce shorter-period oceanographic pressure signals to show the temperature sensitivity more clearly.

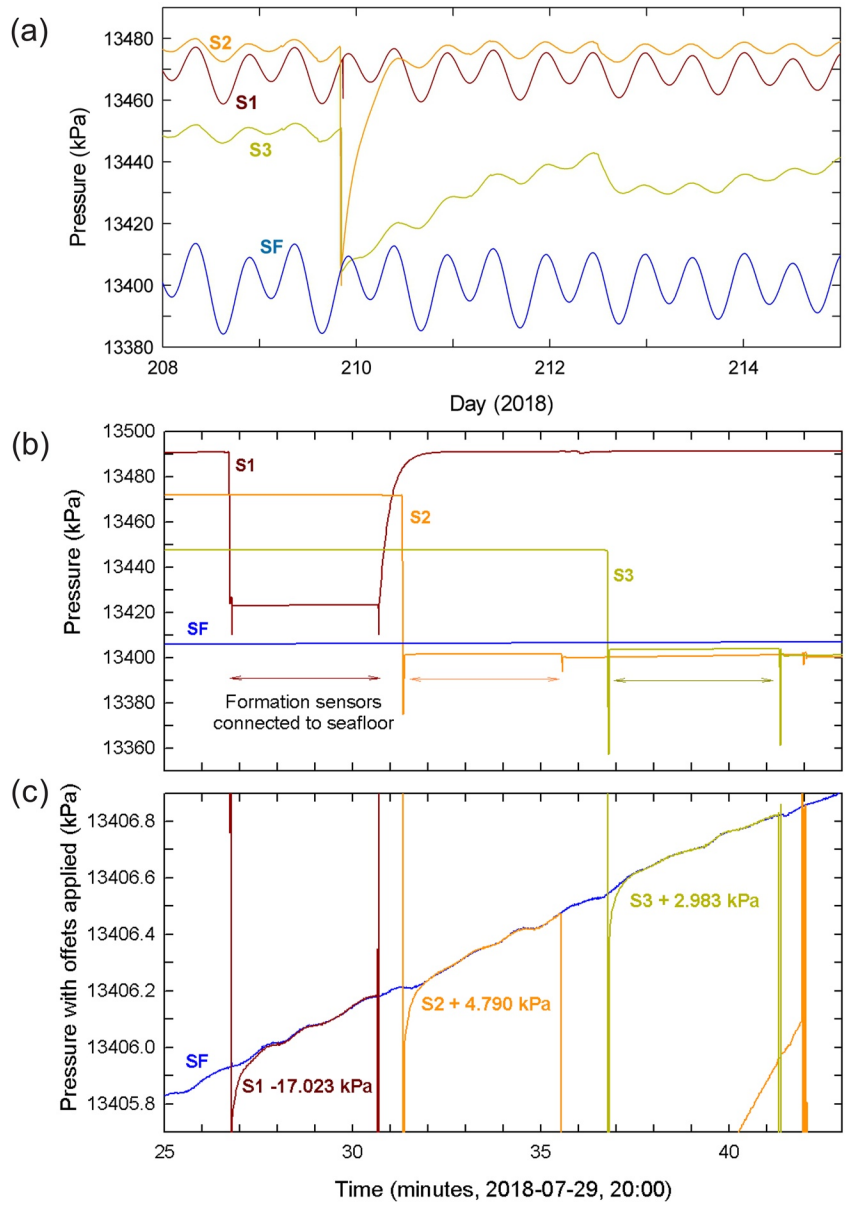

Figure 4. Examples of pressure sensor drift calibration. (a) Seven-day records spanning the hydrostatic calibration check in 2018 show the pressure drop at each sensor at the time of switching the valve to the open ocean, and the recovery after switching the valve back to formation. (b) 18-min records show the details of the 2018 calibration operation. (c) Offsets are applied to the formation-sensor records to align all sensors' readings of the seafloor pressure.

Paroscientific Inc. to ≤0.1% of full-scale range, in this case ≤40 kPa). Inter-sensor offsets of the Site U1364A formation pressures are determined using three-way valves that can be used at the time of the submersible or ROV (remotely operated vehicle) visits to switch the input of the formation sensors to the local ocean bottom pressure (as done permanently in 2011 at level S4). While this is not an absolute calibration, it does establish a precise hydrostatic baseline for the formation readings. Data recorded during one of these calibrations are shown in Figure 4. The relative accuracy achieved is of the order of 1 Pa (e.g., Figure 4c). An inter-sensor calibration was also provided for the early part of the record during the time when the ACORK assembly hung in the water column prior to installation, although this was not as precise (see Figure 4 in Davis & Heesemann, 2012), owing to the acceleration of the hydraulic lines caused by heave, and the temperature dependence of the plumbing fluid density. The first in situ calibration on 30 June 2016, was also compromised, in this case by effects related to the contemporary down-hole seismometer installation. Offsets defined by subsequent calibrations (28 July 2018 and

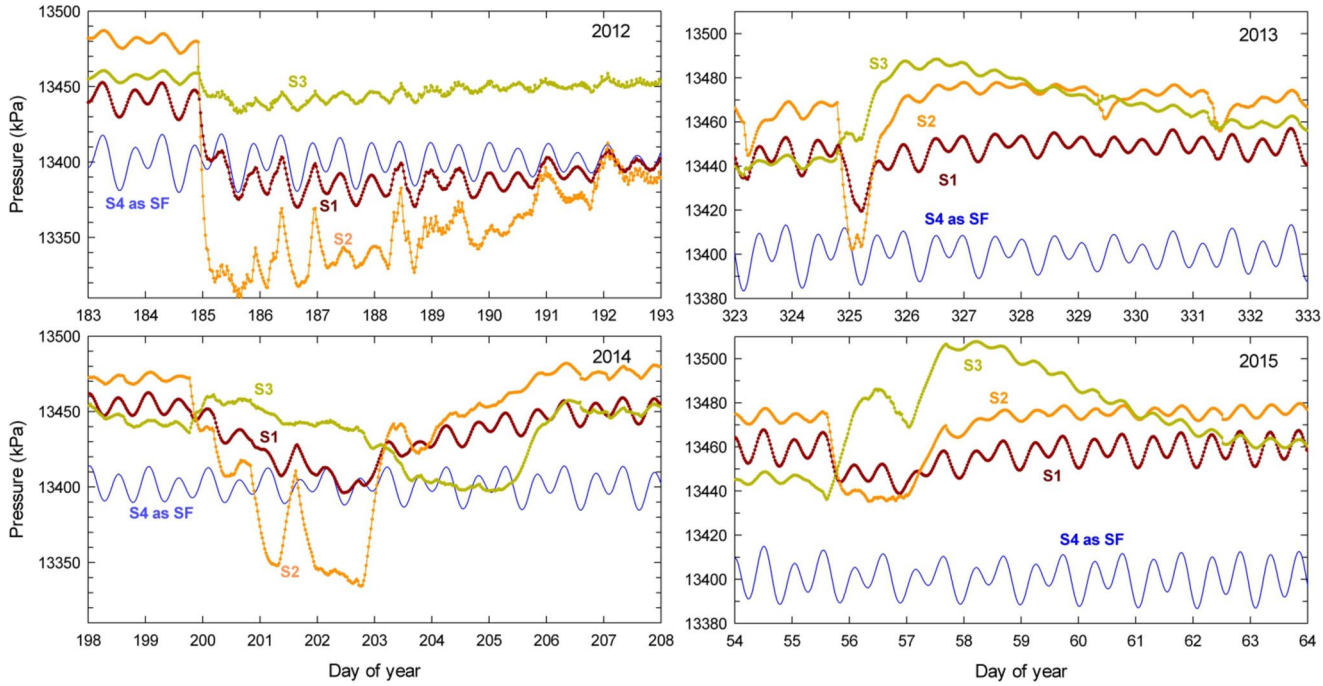

Figure 5. Details of four cases of transient formation pressure excursions (also seen in Figure 2). See Section 3.3 for detailed explanations.

5 September 2019) were within a few tenths of 1 kPa of one another. The sensor drift defined for S1 over the intervening 13-month period was 0.18 kPa yr^{-1}. The corrections determined in 2019 have been applied to all raw values at S1, S2, and S3, as has the offset between the seafloor and S4 sensors observed during deployment to the values of the seafloor sensor, prior to its failure in 2011.

3.3. Pressure Excursions

A discussion of the first 5 months of the data (up to the time of the failure of the original seafloor sensor) was provided by Davis and Heesemann (2012; see Figures 5, 6, and 8 in that publication). Immediately following the time of the ACORK installation, peak pressures (relative to hydrostatic) ranged systematically from +470 kPa at the shallowest screen S4 to +850 kPa at the deepest screen S1, significantly higher than values that would have been associated with the weight of mud used to condition the hole prior to the installation of the ACORK assembly (c. 1,200 kg m^{-3}). Such high pressures were attributed to hydraulic charging of the formation during drilling and insertion of the ACORK casing system. At the time the ACORK was latched in at the wellhead and released from the drill string, pressures dropped to levels close to (in the case of S1) or somewhat below those estimated from the density of the mud used for drilling. Except for transients 7 and 9 days after installation, these dissipated smoothly over the course of roughly 2 weeks to values ranging from +60 to +100 kPa, but over the course of the following several months, large variations returned.

Similar, but smaller synchronized variations at S1, S2, and S3 were present after the restoration of logging in mid-2011, and they continued to occur for several years (Figure 2). The largest excursions early in this period were negative-going, with relatively sharp (hours long) synchronous onsets followed by recoveries over several days or more (Figure 5). The largest amplitudes occurred commonly (but not always) at S2, and in several early instances, pressures fell below hydrostatic. After the first quarter of 2015, variations diminished progressively both in amplitude and frequency of occurrence at S1 and S2 but persisted at S3 with amplitudes of up to tens of kPa until the present time (Figure 2).

Understanding the cause of these anomalies would be useful for gaining confidence in the detection of possible pressure transients caused by deformation associated with seismic or aseismic slip at the base of (or deep within) the accretionary prism. Purely hydraulic causes (e.g., episodes of leakage outside of the casing), or transient fluid migration from greater depth, can be discounted by the occasional occurrence of sub-hydrostatic pressure

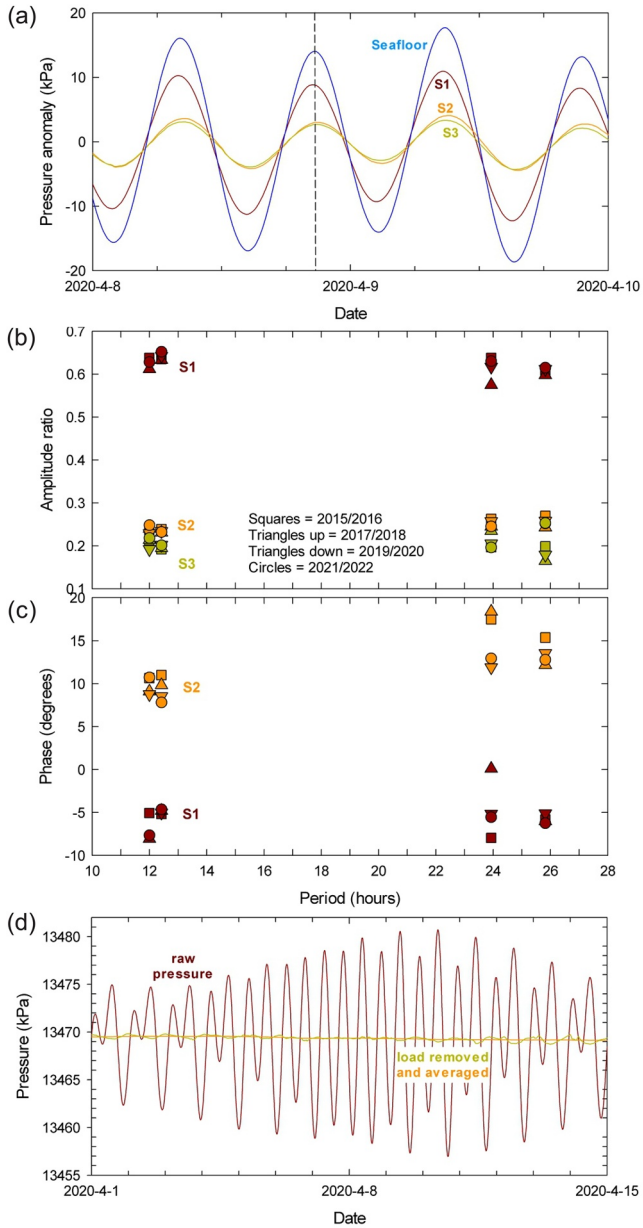

Figure 6. Analysis of formation tidal loading response and the corresponding de-tiding data processing. (a) Pressure records over a 2-day time window showing typical seafloor and formation tidal variations. Dashed black line marks the high tide (wave crest) recorded at the seafloor, showing the slight phase lead at S1 and phase delay at S2 and S3. (b, c) Amplitude and phase of formation tidal signals relative to seafloor loading determined from harmonic analysis using the TAPPY algorithm (Cera, 2011). Results are shown for the strongest tidal constituents O1, K1, M2, and S2 using four 2-month segments of data beginning on December 1 of 2015, 2017, 2019, and 2021. (d) The amplitude and phase results are used to remove formation tidal loading signals. A sequential 24- or 25-hr moving average can be applied to obtain the final "cleaned" signals.

values (e.g., S2 and S3 pressures can be seen occasionally dropping below the seafloor pressure in Figures 2 and 5), by the synchroneity of the excursion onsets among the screens (Figure 5), by the maintenance of average pressure differences and tidal loading signals among screens (Figure 2; see Section 3.4), and by the absence of temporal variations in borehole temperature records during the logging period that spanned several of the pressure excursions (Becker et al., 2020).

One of the most reasonable possibilities is that the perturbations are related to gas migration dynamics, either directly or arising from consequent volumetric strain. Events shown in detail in Figure 5 exemplify a variety of behavior in terms of relative signs and magnitudes of the excursions, and suggest that sources must have a corresponding variety of depths and distances from the screens. The magnitudes of the excursions at S2 and S3 (both near the limiting depth of gas hydrate stability) being largest and the leading offsets at S2 (where free gas is likely present) being negative-going (Figure 5) are consistent with episodic release of gas.

Regardless of the exact cause of the pressure excursions, the progressive decline in their size and frequency of occurrence—from pervasive early on to small at S2 and nearly absent at S1 after mid-2015—is encouraging. It suggests that their cause is not tectonic, and that the latter parts of the records at the deeper two sensors, particularly S1, provide a useful means of tracking any fault-slip-related strain events.

3.4. Tidal Pressure Variations

To search for transients associated with earthquakes or other sources of strain, it is necessary to remove the effects of ocean tidal loading from formation pressure. The general relationship between the seafloor and formation pressure variations has been discussed at length previously (e.g., K. Wang & Davis, 1996; K. Wang et al., 1998). Formation response to seafloor pressure loading can be separated into (a) an elastic (instantaneous) component that depends on the compressibility of the sediment or rock matrix (that at this location may contain solid gas hydrate), the compressibility of the interstitial fluid (that may contain free gas), and porosity, and (b) a diffusional term that depends on the hydraulic diffusivity of the formation and distance over which diffusive signals propagate. The first defines the one-dimensional (1-D) loading efficiency Υ, with $(\mathbf{1}-\Upsilon)$ reflecting the degree to which the formation matrix supports the ocean load. Figure 6a shows an expanded view of data from each of the screens to illustrate the nature of the seafloor and formation tidal signals. At the deepest screen, S1, the tidal signal is attenuated relative to ocean loading by a factor of 0.64, and slightly leads the seafloor signal. In contrast, the ratios of formation to seafloor tidal signals at the two screens above are only about 0.20 and lag those at the seafloor. Proper determinations of phase and amplitude are provided by harmonic analysis targeted at strong tidal constituents (Figures 6b and 6c). Results are consistent from year to year and indicate little or no frequency dependence of formation signal amplitude or phase relative to the seafloor load at S1, lower amplitudes at S2 and S3 relative to those at S1, and possibly some frequency dependence of phase at S2. High levels of noise (discussed in Section 3.3) preclude accurate phase determinations for S3.

Small signal amplitudes at the upper two screens (immediately below and above the limiting depth of gas-hydrate stability) and large phases at S2 may reflect the presence of free gas at S2 (increasing the compressibility of the interstitial fluids), hydrate at S3 (decreasing the compressibility of the sediment matrix), and hydraulic

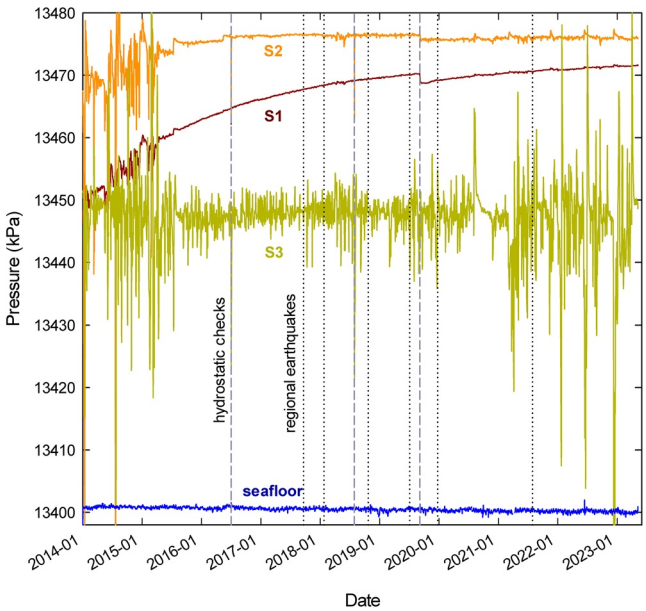

Figure 7. History of Hole U1364A pressure records since 2014 with noise associated with sensor offsets, temperature sensitivity, and ocean loading removed (as described in Section 3). Times of hydrostatic sensor calibration checks are marked by dashed lines, and times of the earthquakes shown in Figure 8 are marked by dotted lines.

diffusion in the vicinity of the gas/gas-hydrate boundary. The attenuation of tidal signal at the deepest screen S1 relative to at the seafloor (i.e., $\Upsilon = 0.64$) is consistent with that seen in subduction-prism sediments elsewhere (e.g., Becker et al., 1997; Davis & Heesemann, 2012; Davis et al., 2009), and with what would be expected for the ~50% sediment porosity at this level (Davis et al., 2009; Riedel et al., 2006). This lithologically reasonable loading efficiency, the lack of frequency dependence, and the small phase suggest that the pressure variations recorded at the deepest screen properly reflect those in the surrounding formation. The absence of complicating factors is also supported by observations for higher-frequency loading, such as ocean infra-gravity waves and seismic ground motion. Sun et al. (2021) and Sun and Davis (2022) have examined the relationship between pressure variations and strain imposed by Raleigh waves (with dominant energy in period of 20–50 s) from distant earthquakes and inferred a matrix compressibility that is consistent with what is derived from the tidal loading response.

The simplicity and temporal stability of the response to seafloor loading permits an easy removal of the seafloor-loading effects from the raw pressure records. This is done by subtracting the seafloor signal—reduced by the observed loading efficiency and time-shifted according to the observed phase at each screen—from the formation signal. Remaining residuals, arising from the second-order effects of shorter-period tidal constituents and hydrologic factors, are removed by applying sequential 24- and 25-hr moving averages. The effectiveness of these steps is illustrated in Figure 6d.

4. Constraints on the Lack of Tectonically Driven Transients at U1364A S1

4.1. Overview

In Figure 7, we show a summary of the processed pressure data since 2014, with the tidal components removed and the calibration offsets corrected using the steps described in Section 3. Compared with the raw records shown in Figure 2, the processed data show more clearly the average pressure state at each monitoring level. Over the period from 2015 to the present, pressures at S1 increase by ~20 kPa with a decaying rate, and remain on average roughly steady at levels S2 and S3 (Figure 7). As seen in the raw data, the long-term trends are perturbed by short-duration fluid pressure excursions at all screens early in the records, but large perturbations persist up to the present time only at S3. Because of the persistent pressure excursions at S3, the record from that screen cannot be applied to the investigation of tectonically driven pressure transients. The quietest record is provided by the deepest level S1 since mid-2015; therefore, in the discussions that follow, we focus on these data and estimate the degree to which they can resolve the state of Cascadia megathrust locking.

A notable exception to the generally monotonic records at the deeper two screens occurred at the time of the hydrostatic calibration operation in 2019 (Figure 7). In all earlier calibration operations, subsequent transients were also observed (such as that illustrated in Figure 4a), but typically with recovery times of just one to a few days. A significant shortcoming of the three-way valves used to switch the sensor hydraulic connections from formation to seafloor is that there is an intermediate state in the switching, when the formation is connected to the open ocean, possibly allowing the expulsion of some finite volume of formation water and free gas. In the case of the 2019 operation, the offsets were roughly 1 and 2 kPa at S2 and S1, respectively, and their recoveries persisted over the course of more than a year.

4.2. Lack of Transient Pressure Variations During Large Earthquakes and Dynamic Stressing

If the subduction megathrust is not completely locked and some slip or creep can occur, dynamic triggering of slip by large earthquakes is possible because of the enhanced dynamic stressing. Examples of dynamically triggered fault failure (including seismicity, tremor, or slow slip) have been reported for many inter- and intra-plate fault zones (e.g., Gomberg et al., 2001; Peng & Gomberg, 2010; van der Elst & Brodsky, 2010). One clear case

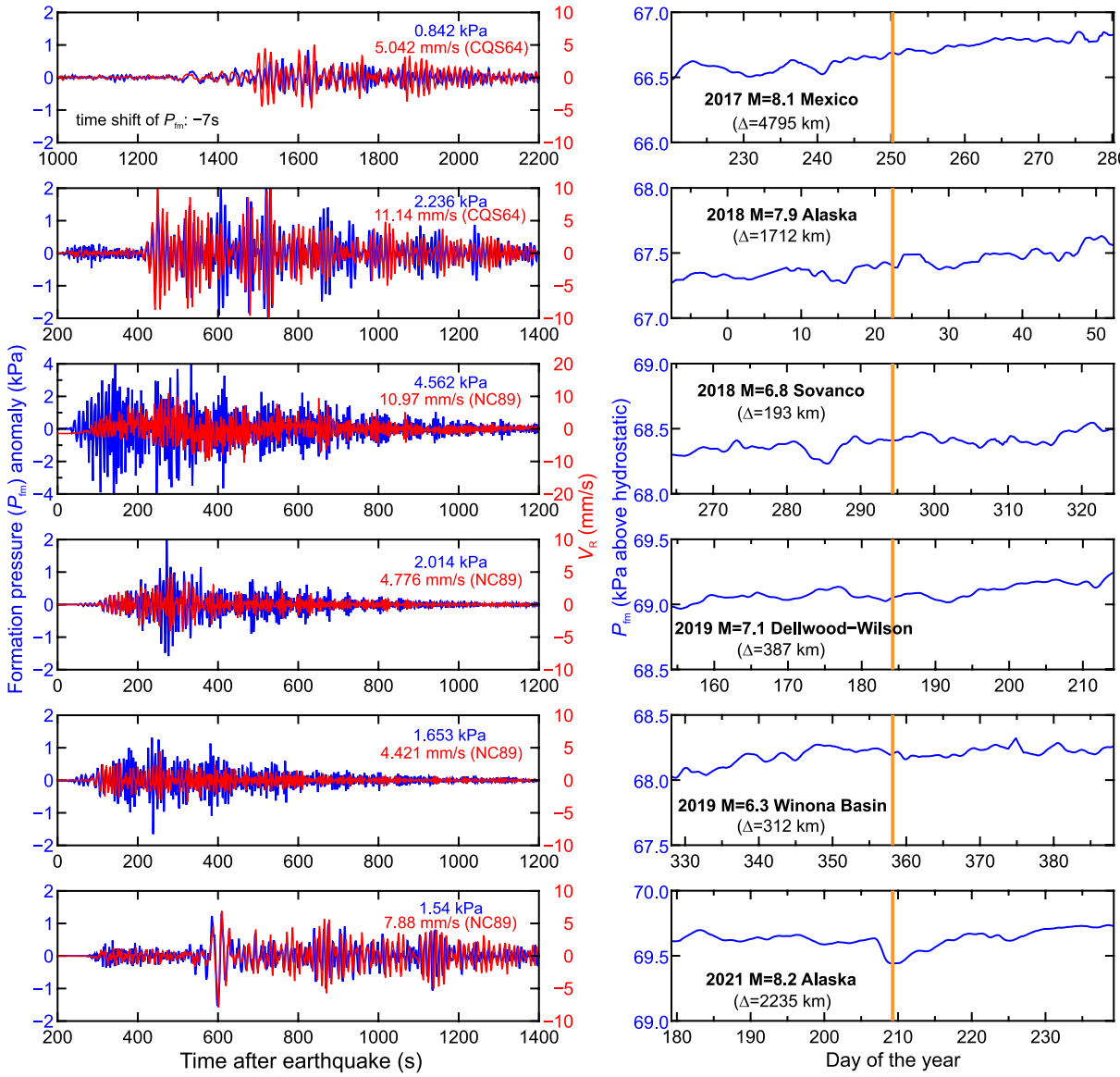

Figure 8. Summary of the response of U1364A S1 formation pressure to dynamic shaking caused by regional and distant large earthquakes. In each row, the left panel shows seismic signals of formation fluid pressure P_{fm} (blue) and radial ground velocity V_R (red) recorded by the collocated (CQS64) or nearby seismometer (NC89, ~3.5 km away), with numbers indicating peak signal amplitudes. A time shift of 7 s was applied to the P_{fm} record, to account for the pressure diffusion time (associated with local lithology and observatory configuration) to optimize the phase agreement between the two signals (Sun & Davis, 2022); the right panel shows pressure anomalies relative to hydrostatic, with tidal and other ocean loading signals and noise removed using methods explained in Section 3, over a longer 2-month period spanning the earthquake origin time (marked by the orange line). No transients or offsets were observed after any of these earthquakes. Δ: earthquake epicentral distance.

for a subduction zone setting is the widespread slow slip along the Northern Hikurangi megathrust triggered by the 2016 M_w 7.8 Kaikoura earthquake (Wallace et al., 2017). For faults subjected to a sub-critical average stress state, dynamic ground motion during the passage of seismic waves may load the faults sufficiently to reach a failure state (Hill, 2008).

An earlier investigation of the presence or absence of local triggered megathrust slip at Northern Cascadia was conducted by McGuire et al. (2018). By using data from downhole instruments over an 8-month period (2015 October to 2016 May) in Hole U1364A, they reported that no tilt anomalies, formation pressure anomalies, or seismic tremor signals were resolved. In that study, particular attention was given to the arrival times of surface waves from three M_w 7.8–8.1 earthquakes at epicentral distances within 1,500–5,000 km that caused sufficiently intense ground shaking to trigger tectonic tremor downdip of the seismogenic zone. Peak ground velocities

caused by these events at U1364A ranged from 1 to 9 mm s^{-1}, and shear stress estimated at the depth of the base of the accretionary prism ranged from 1 to 10 kPa (McGuire et al., 2018). With the substantially extended records now available, it is possible to examine additional events, including the local 2018 $M_w = 6.8$ Sovanco earthquake (Figure 8) that produced a peak ground velocity (and by inference shear stressing at depth) twice as large as that of the 2018 $M_w = 7.9$ Alaska earthquake (the most impactful event examined by McGuire et al., 2018).

Arrivals from this and five other earthquakes are shown in Figure 8, including the U1364A S1 pressure records over two different time windows. Over a short 20-min window that brackets the highest amplitude seismic signals, formation pressure (P_{fm}) variations are shown together with the ground velocity (V_R) recorded in the seismic arrival's radial direction either at the same location (by borehole seismometer CQS64) or nearby (by buried seismometer NC89). For typical surface-wave periods (20–50 s), P_{fm} is loaded primarily by Rayleigh-wave ground motion in the radial direction, with the efficiency of the loading governed by formation matrix's elastic properties (Sun et al., 2021). Over the longer-term 30-day window that brackets the earthquake origin time (marked by the orange line in Figure 8b), the de-tided and processed formation pressure record (using the methods explained in Section 3) demonstrates the absence of any resolvable offsets or transients that would be driven by local tectonic events if they were to exist, despite the large ground velocities and (by inference) dynamic stressing at the times of all of these large earthquakes.

4.3. "Seismic Quiescence" of Cascadia Further Supported by CORK Observations

A widely recognized feature of the present-day Cascadia subduction zone—in striking contrast with other subduction margins—is its extremely low productivity of earthquakes (Bilek & Lay, 2018; Hayes, 2017; International Seismological Centre, 2022; K. Wang & Tréhu, 2016), especially those along the plate interface (Figure 1). During the multiple decades of monitoring with land-based modern instruments at Cascadia, the only major thrust earthquakes detected are two M_w 4.7–4.9 earthquakes offshore of Oregon that are closely related to a local subducted seamount (Tréhu et al., 2012). Recent ocean bottom seismometer (OBS) observations of the Cascadia Initiative project allow some small (magnitude <4) offshore seismicity to be determined (Stone et al., 2018), with most of the resolved events off Oregon (Morton et al., 2018; Tréhu et al., 2015) around the subducted seamount earlier addressed by Tréhu et al. (2012) and off the Mendocino triple junction zone (Gong & McGuire, 2021). For the majority of the Cascadia megathrust including the northern segment off Vancouver Island, however, "seismic quiescence" has been demonstrated by the lack of seismicity along the subducting plate interface during multiple episodes of seafloor OBS monitoring (e.g., Hutchinson et al., 2019, 2020). Seismic activities seem to have been observed only within the subducting plate and the upper-plate continental crust.

However, because of the relatively limited recording bandwidth of seismometers (especially short-period instruments), the interpretation of the observed "seismic quiescence" is left with some ambiguity—either a seismogenic but currently completely locked or a fully aseismic creeping fault can be invoked to explain the absence of seismicity. The latter may be possible for the shallowest fault segment, given recent laboratory studies that suggest a weak and predominantly velocity-strengthening frictional properties of the rock and sediment samples being input to the northern Cascadia subduction zone retrieved from IODP Site U1301 (Stanislowski et al., 2022). Compared to records from either short-period or broadband seismic records, our borehole fluid pressure observations cover significantly wider signal bandwidth that includes slow and static change over many days or even weeks (given the relatively low formation permeability; Davis et al., 2013) and are thus also sensitive to crustal strain caused by purely aseismic slip.

While the useful (low-noise) observations made at Cascadia (Figure 7) span only 8 years and represent a limited along-strike extent (to be quantitatively analyzed in Section 5), the lack of transients stands in stark contrast to observations made with similar borehole observatories elsewhere, namely at the Barbados, Mariana, Costa Rica, Nankai, and Hikurangi subduction zones (Figure 9). Over the comparable to mostly shorter recording periods at each of these margins, multiple deformation events have been observed, with most and possibly all caused by slip on the underlying subduction thrusts. The observed pressure variation patterns and other accompanying geophysical observations (when available) suggest that these slip events could be slow (at sub-seismic slip rates of km/day), could have propagated from greater depths at or near the shallow limit of seismogenesis, and could follow various possible scenarios including being locally spontaneous, being triggered by surface waves from distant large earthquakes, or having followed seismogenic slip deeper along the megathrust. Pressure transient amplitudes range from less than 1 kPa up to 140 kPa, and occur over timescales of several to many days (Figure 9). Any similar slip events, if they ever were to happen at Cascadia during the monitoring period, would be easily detected in the pressure records from sensor S1 or even S2. To what degree the frequency and size of these observed events might be typical is difficult to evaluate with the data in hand, but comparatively speaking, the quiescence of northern

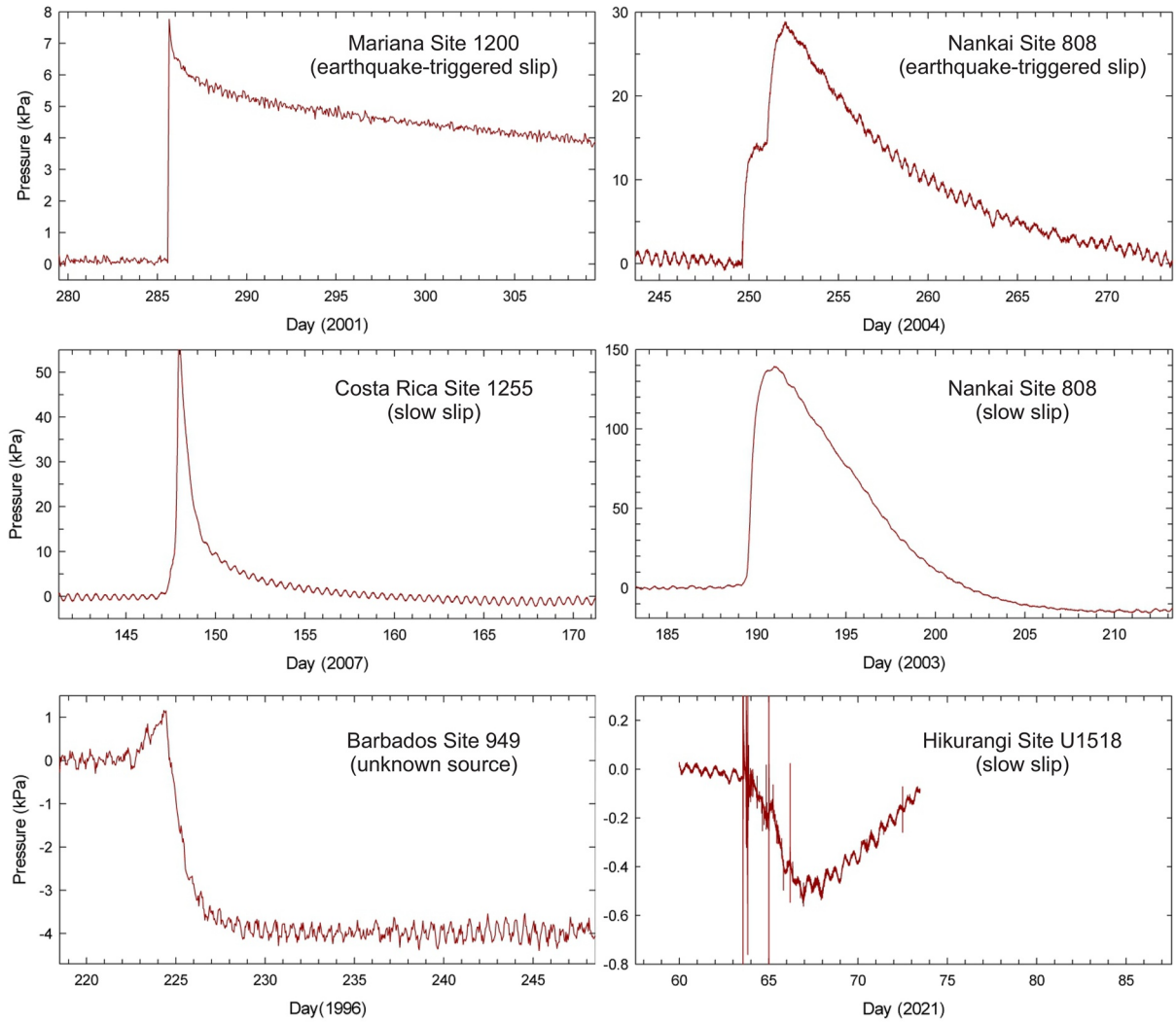

Figure 9. Formation pressure records from CORK borehole observatories at the Barbados, Mariana, Nankai, Costa Rica, and Hikurangi subduction zones, each showing pressure transients possibly due to slip events (either triggered or spontaneous) that have been observed during equivalent or shorter monitoring periods (one to several years) relative to that at Cascadia.

Cascadia (cf., Figures 8 and 9) is noteworthy. The comparison suggests that the Cascadia subduction megathrust in the vicinity of Hole U1364A is likely to be currently fully locked, that is, serving as an "end-member" case of "no slip". Strictly speaking, the transient-free pressure record alone cannot rule out the scenario of a steadily creeping fault, but we deem this scenario unlikely, when considered in context with the lack of dynamically triggered pressure transients (Section 4.2), the lack of regional seismicity along the thrust interface (International Seismological Centre, 2022), the infrequent occurrence of historical Cascadia megathrust earthquakes (Goldfinger et al., 2012), the thermal, lithology, and consolidation state that favors locking and stick-slip along the shallow Cascadia megathrust (Han et al., 2017; Hyndman & Wang, 1993; Tobin, 2022), and the expected effect of "stress shadow" updip of the seismogenic zone (Lindsey et al., 2021; K. Wang & Dixon, 2004). It is worth noting that Chaudhuri and Ghosh (2022) recently reported widespread very low frequency earthquakes (VLFEs) offshore Cascadia using OBS data, but the reported events, if reliable, likely bear little relevance to megathrust slip because of the strike-slip mechanism of most events and the occurrence of some events seaward of the deformation front.

5. Assessing the Resolvable Slip Along the Northern Cascadia Megathrust

The U1364A S1 record with minimal noise (i.e., after mid-2015) offers a unique opportunity to determine the lower limit of the resolvable slip, or in other words, the maximum possible slip magnitude that is not at odds with

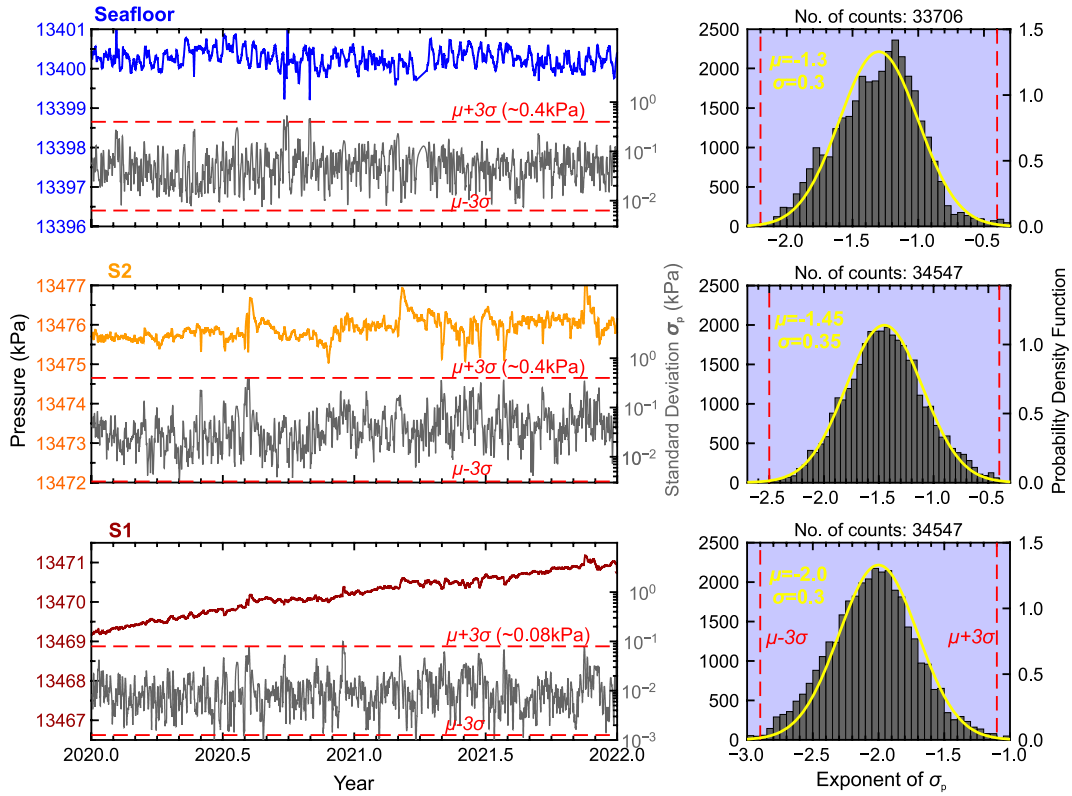

Figure 10. Noise-floor analysis of the pressure records to determine the "threshold" for detecting tectonically driven pressure changes. Left panels show pressure values over a 2-year period, with their standard deviations (σ_p) computed using consecutive 2-day time windows. Red dashed lines show the upper and lower limits of the range of likelihood—with the upper-limit value treated as the "detection threshold." These limits are determined based on the distributions of pressure noise that approximately follow normal (Gaussian) distribution (yellow curves in right panels), with the mean (μ) and standard deviation (σ) provided. Based on probability theory, any values outside the range ($\mu - 3\sigma$, $\mu + 3\sigma$) are "extremely unlikely." Formation pressure S3 record was not analyzed due to the large excursive pressure noise (Figure 7).

the observed anomaly-free pressure record. Any slip events larger than this "resolvable slip" can be ruled out over the observation period, as they would otherwise cause pressure transients that could be confidentially recognized.

5.1. Quantifying the "Detection Threshold" Based on Noise Analysis

To quantify the detection threshold (i.e., resolution limit) for tectonic signals, we conduct simple statistical analysis on the U1364A S1 pressure record to assess its noise-floor level. We calculate the standard deviation of the processed pressure record that is dominated by "noise" due to complex small-scale ocean loading and hydrological perturbations within the formation—both not accounted for with the data processing explained in Section 3. The quantified detection threshold will be used for the modeling of volumetric strain associated with hypothetical megathrust slip in the next section.

Results are shown for a 2-year portion of the data in Figure 10, in which a window length of 2 days is used to obtain the average pressure value and the corresponding standard deviation (square root of the variance) for each time window. Here, the window length of 2 days is chosen based on the typical duration of the onset of strain-related pressure transients observed at other CORK sites (Figure 9). Calculations using other window lengths (ranging from 6 hr to 5 days) yield similar standard deviation values. The standard deviation of S1 pressure shows variable values between 10^{-3} and 10^{-1} kPa, with the frequencies (time scales) of the variations governed presumably by the unaccounted-for oceanographic loading, hydrological formation signals, or gas-related perturbations. Our analysis suggests that the exponents of the temporally variable standard deviation values follow a normal (Gaussian) distribution (Figure 10), and for the S1 record, a mean (μ) of −2.0 and a standard deviation (σ) of 0.3 were resolved. Based on probability theory, we deem a pressure value corresponding

to ($\mu + 3\sigma$)—0.08 kPa—as the "detection threshold" of the S1 pressure signal. This value represents a rather conservative choice of the detection capability because in probability theory, the range between ($\mu - 3\sigma$, $\mu + 3\sigma$) encompasses a probability of 99.73%; values beyond this range are typically deemed to be extremely unlikely (Figure 10). Given a pressure-to-strain conversion coefficient of ~5 kPa/μstrain for typical accretionary-prism sediments of ~50% porosity (e.g., Davis et al., 2009), this pressure "detection threshold" of 0.08 kPa corresponds to volumetric deformation of 16 nanostrain.

Similar noise-floor analysis was also conducted for S2 formation and seafloor pressure records (Figure 10). For these two records, which are generally noisier than S1, a higher value (0.4 kPa) was determined as the detection threshold. For the hydrostatic seafloor pressure, this threshold is equivalent to a vertical seafloor displacement of ~4 cm, somewhat greater than that determined for pressure data recorded at the Hikurangi subduction zone (~1–2 cm; Wallace, Webb, et al., 2016). Use of data from carefully chosen tectonically stable reference sites can help reduce oceanographic noise (Fredrickson et al., 2019; Inoue et al., 2021), and periodic in situ self-calibrations can be done for better constraining long-term sensor drift (Wilcock et al., 2021). Both greatly improve the utility of seafloor pressure observations for deformation studies (e.g., Woods et al., 2022).

5.2. Determining the "Resolvable Slip" Using Simple Dislocation Modeling

Given the location and the dimension of a slip patch along the megathrust, the "detection threshold" quantified in the preceding sub-section can be used to estimate the "resolvable slip," which, for our study area, also represents the maximum possible slip that is allowed by the transient-free S1 pressure record. In this section, we conduct this estimation using the Okada solution (Okada, 1992) that yields internal and surface deformation (displacement and strain) associated with dislocation of a rectangular fault in a uniform-property elastic half-space. By integrating the deformation of many small rectangular sub-faults, we consider a circular shape slip distribution with spatially smooth-tapering slip magnitude that is mechanically and geologically reasonable (see below for details).

We employ the plate-interface geometry of McCrory et al. (2004) along the margin-normal profile crossing Hole U1364A. This slab model was derived by compiling a large number of regional datasets including multiple seismic profiles covering the shallow portion of the Cascadia megathrust, and it has been used by Gao et al. (2018) for evaluating the tsunami scenarios of Northern Cascadia. Other published fault geometries (e.g., Audet et al., 2010; Hayes et al., 2018; McCrory et al., 2012) were also tested, and they do not affect the deformation results much. In our model domain with the flat top boundary, we apply a depth adjustment to the offshore portion of the megathrust following K. Wang et al. (2018), to make sure the fault depth beneath local seafloor reflects the true upper-plate thickness. For simplicity, we ignore any along-strike geometry change and project the same slab profile in the strike direction. This simplified geometry is adequate for approximating the plate-interface geometry of the northern Cascadia subduction fault, which shows little along-strike variation north of 48°N (Figure 12).

We consider three different slip-patch dimensions, with the radius ranging between 10 and 50 km. The largest slip dimension (radius of 50 km) is comparable with those of the SSE documented in the North Hikurangi margin (Wallace, 2020), among which a 2014 SSE (roughly 80 × 100 km in its dimension) has an equivalent moment magnitude of M_w 6.8 (Wallace, Webb, et al., 2016). In comparison, the smallest slip dimension (radius of 10 km) is more consistent with the SSE observed in the off-Kii region of the Nankai Trough subduction zone, where recurring SSEs with a dimension of 20- to 40-km (M_w 5.0–5.6) were reported to occur beneath a transect of borehole observatories (Araki et al., 2017).

Instead of using a uniform-slip patch that produces deformation artifacts, we use a slip distribution that follows a bell-shaped function (P. L. Wang et al., 2013) in both the dip and strike directions. This slip distribution depicts slip that tapers smoothly in all directions, consistent with arguments on fault mechanics and observations of finite fault slip distributions (e.g., Hayes, 2017; Lay, 2015; Scholz, 1998). We divide the circular shape slip into many small sub-faults of 1 × 1 km or 2 × 2 km (for each of which the rectangular-fault Okada solution can be readily used) and sum up the deformation fields of individual sub-faults to obtain the total deformation field. Figure 11 shows the modeled deformation for the three different slip-patch sizes, located at two different depths to form various buried and trench-breaching slip scenarios.

With the slip center located at 50 km from the trench where the fault depth is about 15 km, all three slip patches produce contraction (and formation pressure increase) in the updip near-trench region (representative of the

observatory site) everywhere along strike (as shown by the "Borehole" profile). The exact magnitudes of the strain and pressure perturbations depend on the slip amount, the slip-patch size, and the along-strike separation of the slip and the borehole. For example, for a large 50-km-radius slip patch that is located directly downdip of the borehole, a peak slip of 1 cm could produce a pressure increase of ∼0.3 kPa (equivalent to a formation contraction of 0.06 μstrain), greater than the "detection threshold (0.08 kPa)" by a factor of ∼4. Hence, a linear scaling down of the deformation field suggests a local resolvable slip as small as <0.3 cm (Figure 11a). This resolvable slip increases with the along-strike separation of the slip and the borehole, reflecting a decreasing detection sensitivity as the expected deformation signal reduces (Figure 11a right two panels). For smaller slip-patch dimensions, our borehole is sensitive to slip within a more limited along-strike extent (Figures 11b and 11c). A similar pattern of the "resolvable slip" is obtained for hypothetical shallow (possibly trench-breaching) slip patches, with the borehole likely to be located in the dilatation (formation pressure drop) domain (Figures 11d–11f). For very shallow slip directly beneath the borehole, the model tests suggest that the pressure monitoring could resolve very small slip of <1 cm for all the slip-patch sizes tested (Figures 11d–11f).

We summarize the results of dislocation models by systematically compiling the three slip-patch sizes at different depths into Figure 12 to provide a quantitative description of the distribution of resolvable slip of our single-site observatory. Despite the limits imposed by having observations at only the single site, the record is able to resolve slip magnitude of ∼10 cm at a distance of 100 km from the "central track", over an extent that is comparable with the size of Vancouver Island, for the hypothetical Hikurangi-type SSE. Resolvability for small-size SSE (e.g., the hypothetical Nanaki off-Kii type) achieves a very high sensitivity to slip directly downdip of the borehole site, reaching as low as 0.1 cm, but it drops rapidly moving away from the "central track" (Figure 12 lower panel).

In summary, the model results shown in Figure 12 suggest a great potential for sub-seafloor fluid pressure monitoring to detect the offshore slip over a rather broad extent centered around the borehole site. Future installations of similar borehole observatories, which require only a few in number but with their locations wisely chosen along the strike, may offer a great coverage for the entire Cascadia megathrust.

6. Discussion

6.1. Effect of Spatially Variable Upper-Plate Rigidity

Subduction zone upper-plate materials feature heterogeneous mechanical properties, among which the rigidity progressively increases landward and with depth (e.g., Sallarès & Ranero, 2019). For accretionary margins such as northern Cascadia, this landward rigidity increase is primarily due to the progressively enhanced sediment consolidation associated with the increasing overburden and lateral tectonic compression (Bray & Karig, 1985; Saffer & Tobin, 2011; Sun et al., 2020). For erosional margins, the landward rigidity increase is also associated with a spatially variable upper-plate fracturing state (Sallarès & Ranero, 2019). Recent studies suggested the importance of considering realistic spatially variable rigidity in estimating the source slip from observed crustal deformation (e.g., Langer et al., 2023; Williams & Wallace, 2018) and in characterizing deformation and tsunamigenic potential of subduction earthquakes (e.g., Prada et al., 2021; Ulrich et al., 2022).

Here, we conduct a quantitative evaluation of the effect of heterogeneous upper-plate rigidity on the determination of the "resolvable slip" of the present study. We employ the finite element code PGCviscl-3D, which allows the incorporation of spatially variable upper-plate properties. Technical details of the finite-element mesh and modeling methods can be found in Carvajal et al. (2022), who used the same code for a modeling study of subduction zone earthquake and tsunami processes. In Figure 13, we compare the modeled deformation fields of two contrasting scenarios that employ uniform versus heterogeneous upper-plate rigidities, each with the same assigned slip distribution. In the heterogeneous scenario, we allow rigidity to progressively increase from 5 GPa near the deformation front to 48 GPa further inland, over a depth range of 20 km along the base of the upper plate, following the pattern summarized by Sallarès and Ranero (2019) using many seismic velocity observations worldwide.

The deformation comparison in Figure 13 is consistent with earlier studies such as Williams and Wallace (2018) in demonstrating that the surface displacement can be substantially affected by changing the rigidity. Specifically, given the assigned extent of slip, the incorporation of the realistic rigidity variation would enhance the horizontal seafloor motion above the slip area by ∼20%–30% but lead to less near-trench uplift and inland subsidence by ∼10%–20% (see also synthetic tests in Williams & Wallace, 2018). What is more closely related to our formation pressure observation is the sub-surface strain distribution. By incorporating the heterogenous rigidity, the general pattern of the strain field—particularly the transition from frontal contraction to inland dilatation—is not altered,

10.1029/2023GC010910

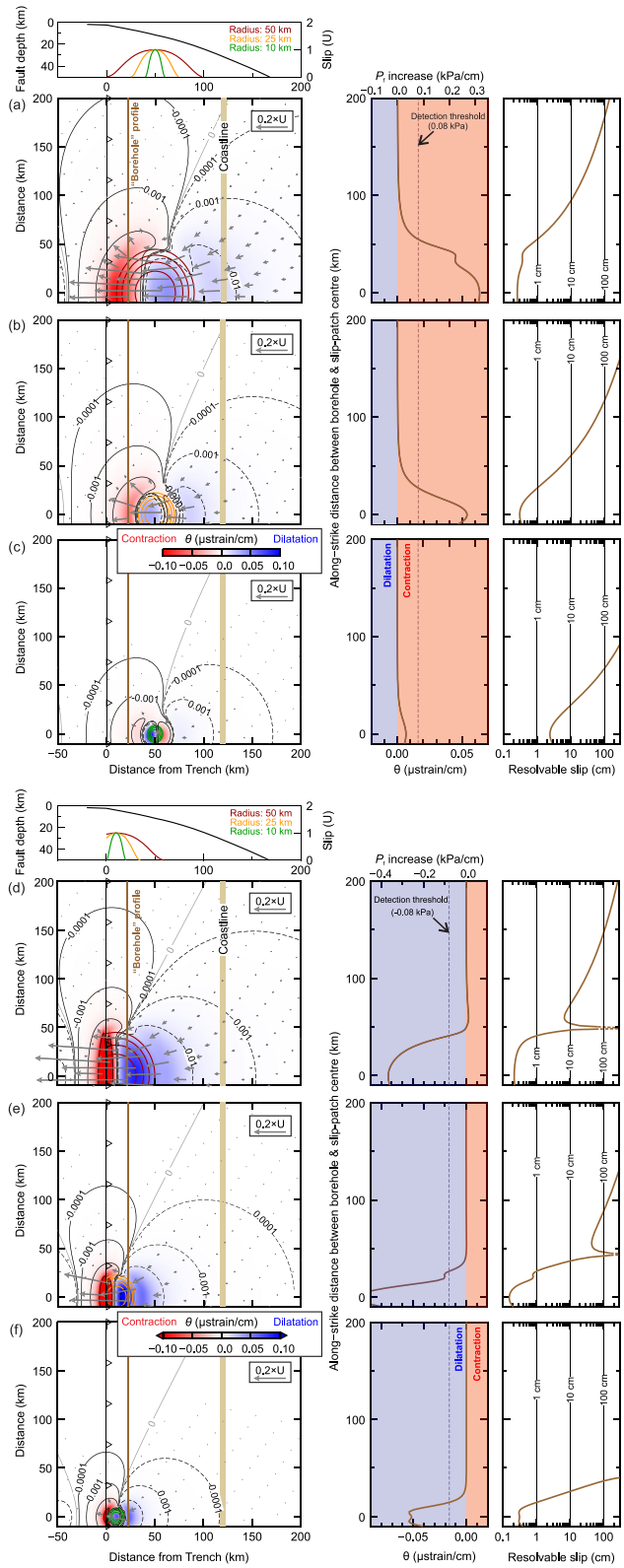

Figure 11.

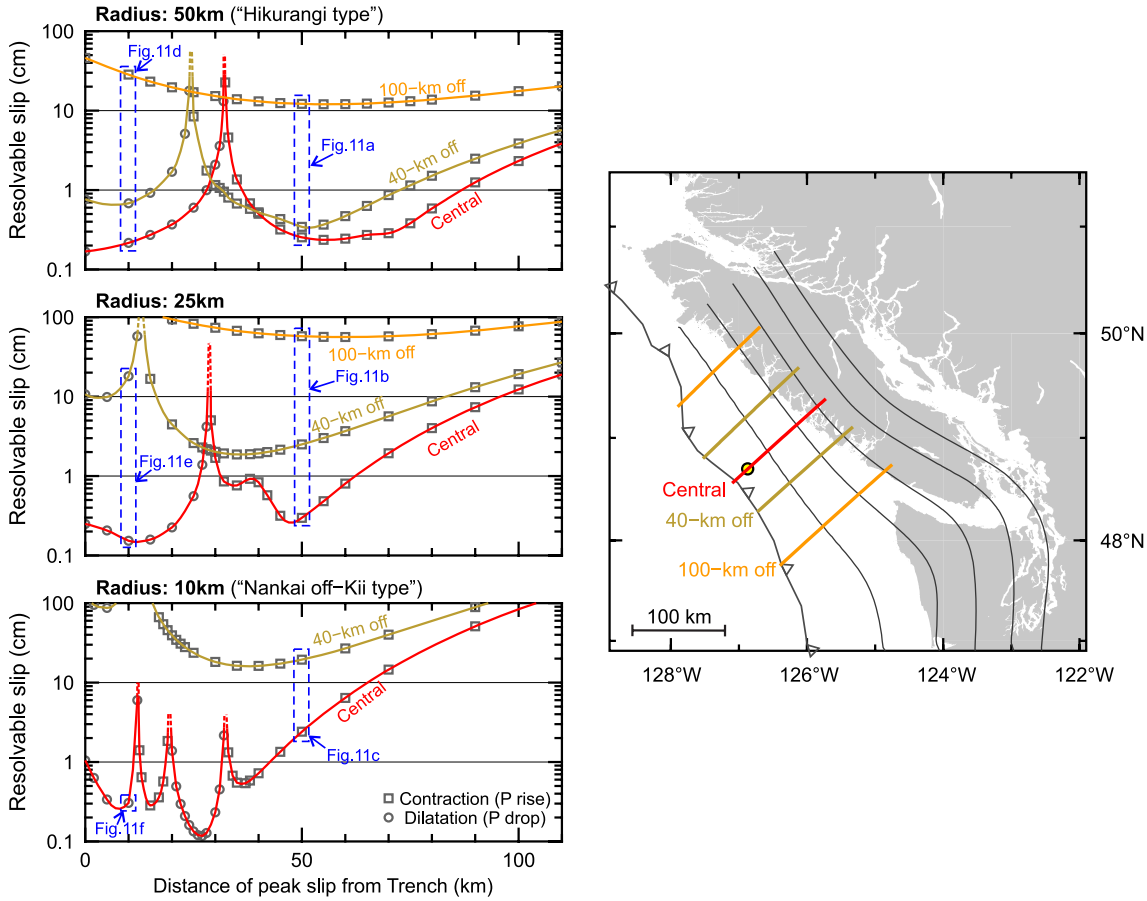

Figure 12. Magnitude of "resolvable slip" and the sense of expected formation pressure anomaly (representing contraction or dilatation), for slip patches along several trench-normal profiles around Hole U1364A. The three different slip patch sizes (see examples in Figure 11) were chosen to illustrate a range of slip event sizes that have been documented at other subduction zones, for example, 50-km-radius slip similar to those observed in N Hikurangi (Wallace, Webb, et al., 2016) and 10-km-radius slip comparable to those in Nankai off-Kii area (Araki et al., 2017). Directly beneath the borehole site, minimal shallow slip as small as <1 cm can be resolved for the wide range of slip-patch sizes (shown by the red lines). 100-km along strike from the borehole site, ~10 cm slip is still resolvable if the slip patch size has a radius of 50 km. Dashed blue boxes denote the set of the models shown in Figure 11. Black lines in the right panel show slab-surface depth at 10-km contour interval (McCrory et al., 2004).

but the strain magnitude is enhanced by ~50% in the near-trench area because of the less-rigid and easier-to-deform frontal upper-plate material. This simple test suggests that strain signals can be more efficiently generated by a given shallow slip patch when considering a more realistic rigidity structure in comparison with the deformation results shown in Figures 11 and 12 assuming uniform elastic properties. Hence, our conclusion regarding the high detection sensitivity of the borehole observatory in resolving the local slip is further strengthened.

6.2. The High Sensitivity of Borehole Pressure Monitoring

Our study serves as a good example for illustrating the very high sensitivity of borehole pressure monitoring for detecting offshore slip. In comparison with other seafloor geodetic tools, it shows advantages regarding both the

Figure 11. Dislocation modeling test of hypothetical circular-shape slip for quantifying the expected formation pressure signal and for determining the "resolvable slip." (a–c) Models of moderately buried slip (at ~15 km beneath surface) with different slip-patch dimensions (radius 10–50 km) assigned to the plate-interface fault (black line in the top panel). Maps in the left panels show volumetric strain at zero depth associated with the slip (contoured at every 0.2 peak slip). Negative (red) indicates contraction (pressure rise), and positive (blue) indicates dilatation (pressure drop). Gray vectors show modeled horizontal surface displacement, with U representing the amount of the maximum slip. "Borehole" profile (brown line) represents all possible along-strike borehole location relative to the slip patch. Right two panels show (1) modeled volumetric strain and formation pressure change along the "Borehole" profile, normalized by peak slip magnitude of 1 cm, and (2) the "resolvable slip" along the same profile, based on linearly scaling (up or down) the deformation field to exactly match the pressure "detection threshold" of 0.08 kPa. (d–f) same as (a–c) but for shallower slip patches. Dashed segments in the rightmost panels show the resolvable slip approaching infinity, which occurs when the borehole is located where the strain caused by the slip patch is zero.

10.1029/2023GC010910

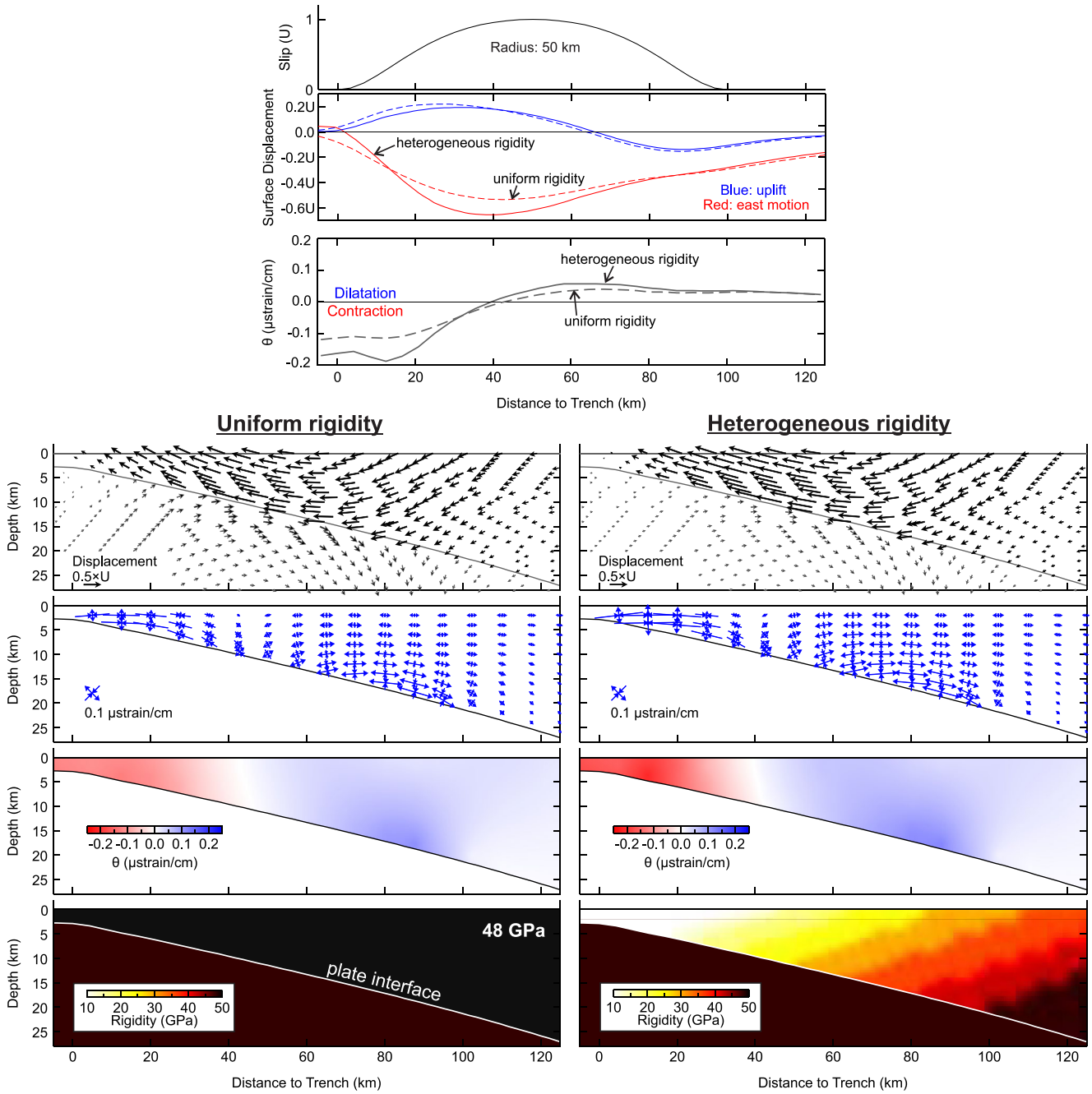

Figure 13. Comparison of two two-dimensional finite-element models with the same slip but different (uniform vs. heterogeneous) upper-plate rigidity distributions for showing the effect of spatially variable upper-plate rigidity on the deformation field and, by inference, the determination of resolvable slip. The lowest two panels show the rigidity distributions; in the "heterogenous rigidity" model, a landward progressive increase of the upper-plate rigidity (over the range of 5–48 GPa) is assumed, following the pattern summarized by Sallarès and Ranero (2019). Above that, panels show (a) the assigned slip, (b) horizontal and vertical surface displacements, (c) sub-surface volumetric strain at 1 km depth, (d) cross section of displacement fields, (e) cross section of deviatoric strain vectors, and (f) cross section of volumetric strain distributions of the two models, both normalized to 1 cm peak slip. In the illustrations of the volumetric strain field, red (negative) indicates contraction (formation pressure increase), and blue (positive) indicates dilatation (formation pressure drop), as in Figure 11.

handling of oceanographic noise and the nature of the detected signal. Existing borehole pressure observatories (Davis et al., 2018) typically employ an accompanying seafloor pressure sensor, which serves as an important reference for removing ocean loading noise. In the absence of hydrologic perturbations, the residual formation signal provides a relatively pure reflection of the formation strain—over a sufficiently local scale to provide sensitivity to any spatial gradient and temporal migration of the source slip. Our dislocation tests in the present study

suggest a high detection sensitivity of borehole pressure monitoring for local slip as small as <1 cm. While no signals are seen at the Cascadia site, the capability of resolving small-to-medium sized shallow SSEs has been well demonstrated at Nankai (Araki et al., 2017; Davis et al., 2013) and Costa Rica (Davis et al., 2015).

This level of sensitivity is in general higher than that of other seafloor geodesy tools by one to two orders of magnitude, in terms of the magnitude of slip that can be resolved. As an example, ocean bottom pressure observations are able to detect deformation via vertical seafloor displacement, but eliminating oceanographic data noise is known to be difficult (as shown by the noise-floor analysis of seafloor pressure in Figure 10). Recent advances in the observational techniques and the theoretical understanding of oceanographic pressure variations (Fredrickson et al., 2019; Inoue et al., 2021; Wilcock et al., 2021) greatly help to improve the noise reduction of seafloor pressure monitoring, however, but with the typically small fault dip of offshore shallow megathrusts, and the reduced sensitivity of uplift in the presence of low outer prism rigidity (see Section 6.1), the generation of a detectable deformation signal often requires a relatively large slip. To date, geodetic applications of seafloor pressure monitoring have resolved slip magnitudes on the order of 10 s of centimeters (e.g., Ito et al., 2013; Sun, Davis, et al., 2017; Wallace, Webb, et al., 2016; Woods et al., 2022).

Despite the advantageously high detection sensitivity, the requirement for ocean drilling, the expense of borehole installations, and the expense and complications associated with remote operations (via submersible or ROV) or cable connections will always limit the wide application of borehole observatories. Thus, any observation network will necessitate a mixture of borehole and seafloor seismic and geodetic tools, with the configuration and site distribution optimized for evaluating deformation over times leading up to, during, and following a megathrust earthquake or other slip behavior.

6.3. Technical Considerations

A distinct characteristic of the Hole U1364A observatory, in reference to others, is its proximity to known accumulation of free gas within the accretionary prism at Cascadia. Indications of gas (e.g., a seismically imaged bottom-simulating reflector) have not been seen in the vicinity of monitoring screens at other sites, and many of the other sites have been completed with greater screen depths (Davis et al., 2018). The distribution of screens at Hole U1364A was originally chosen in part to study gas-hydrate dynamics, for example, to detect vertical hydrologic diffusion above and below the gas-hydrate stability boundary. For the purpose of detecting tectonic strain signals, this appears to have had the unfortunate consequence of undesired pressure variations. These variations were greatest at the shallower screens (S3 and S2), rendering their data quality poor for the purposes of strain monitoring. While present during the first few years of monitoring at the deepest screen (S1), the noise at this depth subsequently became sufficiently small for the formation pressure to provide high sensitivity for detecting tectonic strain (with a detection threshold of ∼0.08 kPa—equivalent to 16 nanostrain—determined from the statistical analysis presented in Section 5.1). From this experience, it is clear that to observe tectonically driven formation pressures with the greatest resolution, levels containing gas must be avoided. The Hole U1364A monitoring screen S1 at 303 mbsf (73 m below the local limit of gas hydrate stability) appears to be just deep enough for it to be useable for strain monitoring, although even late in the monitoring period reported here, some excursions do appear. This is illustrated in Figure 14, where three anomalies are seen at S1 with amplitudes of 0.2–0.3 kPa (in late August, mid-September, and early December 2022)—greater than the estimated event detection threshold of 0.08 kPa. All three are closely correlated with larger excursions at S2 and S3, and like those seen earlier in the record (e.g., Figure 5), they most likely reflect gas dynamics in the upper part of the sediment section. Just as in the case of earlier excursions, the possibility of reflecting any plate-boundary slip is excluded by the contrasting signs between the monitoring screens and the sometime sub-hydrostatic pressure values at S3.

Positioning screens at greater depths would likely have prevented this problem. For example, the deepest monitoring screen within the sediment section arriving at the Nankai accretionary prism (563 mbsf in Hole 1173B) is characterized by a tidal loading efficiency of 0.57, and a pressure noise floor (calculated using the method described in Section 5.1) of ∼0.055 kPa—lower than that of U1364A S1 (∼0.08 kPa). In addition, the lower formation porosity of ∼40% surrounding that monitoring screen (at Nankai Hole 1173B) results in a higher strain-to-pressure conversion coefficient, which aids in both the detection of static and dynamic (seismic) strain (Davis et al., 2013). Another advantage coming with the lower formation porosity at greater monitoring depths is the lower permeability and the greater hydrologic distance to the seafloor. Both help to reduce hydrologic drainage and allow slow accumulation of interseismic strain to be more easily captured. Secular rising trends in

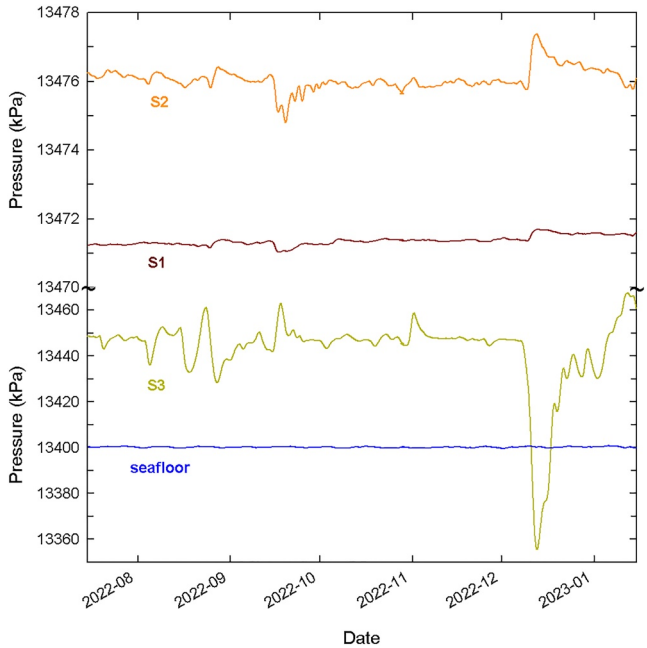

Figure 14. Six-month records of pressure at all monitoring levels in Hole U1364A. Three excursions are present at S1 with amplitudes greater than the statistically determined noise threshold of 0.08 kPa (in late August, mid-September, and early December 2022). All three are correlated with larger anomalies at S2 and much larger anomalies at S3. A change of scaling is employed to allow the full magnitude of the S3 excursion in early December 2022 to be seen.

formation pressure, possibly arising from interseismic contractional strain, have been observed at the Nankai and Costa Rica subduction zones (Davis et al., 2013, 2015). The rising trend seen over the most recent few years at the deepest screen at Cascadia (Figure 7; c. +0.65 kPa yr^{-1}, which is greater than the sensor drift of +0.18 kPa yr^{-1}) may also be a secular tectonic signal, although in this case, the rising trend is diminishing and the cause is more likely to be a long-term recovery following the drilling perturbation.

Another noteworthy lesson learned from the U1364A observatory is that the three-way valve operations for hydrostatic checks may cause unwanted problems. The valves at the wellhead are not "ideal" zero-volume valves, and during their rotation, there is an intermediate state in which the formation is briefly connected to the ocean. The consequence of this "leakage" is seen in the formation pressure records following all calibration operations, as exemplified in Figure 4a—where slow recovery after returning the valve to the formation position is seen at S2 and S3 (over the course of several days). Any leakage should be momentary, and the volume of water lost should be small, but even a small amount of venting can be problematic in the case of low formation permeability or in cases where gas is present. An alternate configuration that would avoid this issue is to employ two-way valves in series, although the added complexities of the plumbing and wellhead operations would add potential risk. Given that the observed relative sensor offsets are modest compared with the absolute magnitudes of overpressure (17 kPa maximum vs. c. 70 kPa, respectively), and that rates of inter-sensor drift are low (tenths of 1 kPa yr^{-1}), it may be best simply to forgo the inter-sensor calibrations, except in cases where precise determination of small absolute pressure signals is desired.

7. Conclusions

In this paper, we report multi-depth formation and seafloor pressure data collected since 2010 by an ACORK observatory installed in IODP Hole U1364A, located roughly 20 km landward of the deformation front of the northern Cascadia subduction zone. After reducing data noise caused by oceanographic and hydrological processes, we study the pressure signals, in conjunction with synthetic deformation modeling, to search for or infer the absence of any possible slip along the underlying subduction megathrust. Our key findings are summarized as follows.

1. Formation pressure records from all depth levels are plagued by unanticipated noise during the first 5 years of the monitoring, likely caused by complex gas dynamics near the local gas-hydrate stability boundary. Noise at the deeper two levels largely abated after mid-2015, however, and the subsequent data—in particular those from the deepest level S1—are of sufficiently high quality for detecting possible tectonically driven pressure signals (Figure 7).
2. Over the 8-year period since the abatement of excursive pressure noise at S1, no transient pressure variations were observed, including at the times of regional and distant large earthquakes that would cause significant dynamic stressing along the local fault (Figure 8). This transient-free record further strengthens the conclusion of no dynamic triggered slip of McGuire et al. (2018) and stands in distinct contrast with observations made by similar CORK systems at six other subduction zone locations (Figure 9). The lack of pressure perturbations reinforces the "seismic quiescence" of the shallow Cascadia megathrust, suggesting its uniqueness in producing no small earthquakes or creep at the current "late inter-seismic" stage, despite known episodic slow slip downdip of the seismogenic zone.
3. Statistical analysis of the noise floor of the S1 pressure record suggests a detection threshold for tectonic signals of 0.08 kPa, equivalent to a strain threshold of 16 nanostrain for typical shallow accretionary-wedge sediments (Figure 10). Simple dislocation models using local fault geometry suggest that this detection capability is able to resolve local slip as little as <1 cm (Figure 11). This "resolvable slip" is much smaller than the range of slip magnitudes reported in earlier studies utilizing other geodetic methods such as monitoring of ocean bottom pressure for vertical seafloor motion or land-based geodetic observations such as GNSS.

4. Our compilation of dislocation models that systematically adopt possible along-strike and along-dip locations of a hypothetical circular slip patch of variable sizes suggests that the single-site observatory is able to resolve slip over a promisingly wide extent in the strike direction (Figure 12). For large slip patches (of a radius of ∼50 km) similar to the SSEs observed at North Hikurangi, the borehole monitoring can resolve 10 cm slip from ∼100 km away, hence covering an along-strike range that is nearly comparable to the size of Vancouver Island. For small slip patches (of a radius of ∼10 km), a more limited range is covered in the strike direction, but a remarkably high detection capability for local shallow slip can be achieved, with a "resolvable slip" down to a few mm. Such high detection sensitivity and the outcome of no detection over our 8-year transient-free record indicate that the Northern Cascadia megathrust has been fully locked during this monitoring period.

Conflict of Interest

The authors declare no conflicts of interest relevant to this study.

Data Availability Statement

Formation and seafloor fluid pressure data from IODP Hole U1364A CORK used in this study are accessible through the Ocean Networks Canada data portal website (https://data.oceannetworks.ca/DataSearch?locationCode=CQS64&deviceCategoryCode=CORK). We note that the archived data include periodic spikes during the first 6 months of 2017 recording that were caused by regular ground-fault checks of the Woods Hole Oceanographic Institution borehole instruments; those and spikes of other origins elsewhere in the history of recording have been detected and replaced by interpolation. Seismic data shown in Figure 8 are archived at the Incorporated Research Institutions for Seismology (IRIS) and are accessible through the IRIS Data Management Center (http://ds.iris.edu/wilber3/find_event), with USGS event names: usgs:us2000ahv0 (2017 M = 8.1 Mexico earthquake), usgs:us2000cmy3 (2018 M = 7.9 Alaska earthquake), usgs:us1000hfgv (2018 M = 6.8 Sovanco earthquake), usgs:us700049sf (2019 M = 7.1 Dellwood-Wilson earthquake), usgs:us70006qt7 (2019 M = 6.3 Winona Basin earthquake), usgs:ak0219neiszm (2021 M = 8.2 Alaska earthquake).

Acknowledgments
Drilling of Hole U1364A and installation of the ACORK infrastructure were carried out by the Integrated Ocean Drilling Program using D/V JOIDES Resolution. We thank the officers and crews of the JOIDES Resolution, RV Tully, RV Sikuliaq, and RV Nautilus, and the research submersibles Jason, ROPOS, and Hercules for their outstanding support of wellhead service operations, data downloads, and cable connections. R. Meldrum provided technical support for the construction and deployment of pressure and seismic instrumentation. T. Pettigrew led the foundational engineering behind the ACORK system. Pressure sensors were built by Paroscienfic Inc., and the high-precision sensor-frequency counters and data loggers by Bennest Enterprises Ltd. and Minerva Technologies Ltd. Support for the ACORK infrastructure (casing, screens, hydraulic umbilicals, reentry cone) was generously provided by IODP with funding from the U.S. National Science Foundation. Support for the pressure-monitoring instrumentation and post-installation wellhead operations was provided by Ocean Networks Canada and the Geological Survey of Canada. All authors have received support for their time from their home institutions, with additional support provided to KB from the National Science Foundation (Grant OCE-1259718). L. Wallace and D. Saffer kindly granted permission to include the Hikurangi example shown in Figure 9. Jiangheng He developed the finite element code PGCviscl-3D that is used in the deformation model tests presented in Section 6.1. We thank Roland Bürgmann and Laura Wallace for valuable review comments and Kelin Wang for providing an internal review. This is Geological Survey of Canada contribution 20220670.

References

Araki, E., Saffer, D. M., Kopf, A. J., Wallace, L. M., Kimura, T., Machida, Y., et al. (2017). Recurring and triggered slow-slip events near the trench at the Nankai Trough subduction megathrust. *Science*, *356*(6343), 1157–1160. https://doi.org/10.1126/science.aan3120

Atwater, B. F., Nelson, A. R., Clague, J. J., Carver, G. A., Yamaguchi, D. K., Bobrowsky, P. T., et al. (1995). Summary of coastal geologic evidence for past great earthquakes at the Cascadia subduction zone. *Earthquake Spectra*, *11*(1), 1–18. https://doi.org/10.1193/1.1585800

Audet, P., Bostock, M. G., Boyarko, D. C., Brudzinski, M. R., & Allen, R. M. (2010). Slab morphology in the Cascadia fore arc and its relation to episodic tremor and slip. *Journal of Geophysical Research*, *115*(B4), B00A16. https://doi.org/10.1029/2008jb006053

Audet, P., & Schaeffer, A. J. (2018). Fluid pressure and shear zone development over the locked to slow slip region in Cascadia. *Science Advances*, *4*(3), eaar2982. https://doi.org/10.1126/sciadv.aar2982

Bartlow, N. M. (2020). A long-term view of episodic tremor and slip in Cascadia. *Geophysical Research Letters*, *47*(3), e2019GL085303. https://doi.org/10.1029/2019gl085303

Becker, K., Davis, E. E., Heesemann, M., Collins, J. A., & McGuire, J. J. (2020). A long-term geothermal observatory across subseafloor gas hydrates, IODP hole U1364A, cascadia accretionary prism. *Frontiers of Earth Science*, *8*, 568566. https://doi.org/10.3389/feart.2020.568566

Becker, K., Fisher, A. T., & Davis, E. E. (1997). The CORK experiment in Hole 949C: Long-term observations of pressure and temperature in the Barbados accretionary prism. In Y. Ogawa, T. Shipley, P. Blum, & J. Bahr (Eds.), *Proceedings of the Ocean Drilling program. Scientific results* (Vol. 156, pp. 247–252).

Bilek, S. L., & Lay, T. (2018). Subduction zone megathrust earthquakes. *Geosphere*, *14*(4), 1468–1500. https://doi.org/10.1130/ges01608.1

Bray, C. J., & Karig, D. E. (1985). Porosity of sediments in accretionary prisms and some implications for dewatering processes. *Journal of Geophysical Research*, *90*(B1), 768–778. https://doi.org/10.1029/jb090ib01p00768

Bürgmann, R. (2018). The geophysics, geology and mechanics of slow fault slip. *Earth and Planetary Science Letters*, *495*, 112–134. https://doi.org/10.1016/j.epsl.2018.04.062

Bürgmann, R., & Chadwell, D. (2014). Seafloor geodesy. *Annual Review of Earth and Planetary Sciences*, *42*(1), 509–534. https://doi.org/10.1146/annurev-earth-060313-054953

Carbotte, S. M., Boston, B., Han, S., Shuck, B., Canales, J. P., Beeson, J. W., et al. (2022). New observations of plate interface depth and geometry at the offshore Cascadia subduction zone from the CAscadia Seismic Imaging Experiment 2021 (CASIE21) and comparisons with existing plate depth models. In *Abstract S46B-01 (Fall Meeting, AGU, Chicago, 12–16 December 2022)*. Retrieved from https://agu.confex.com/agu/fm22/meetingapp.cgi/Paper/1122317

Carvajal, M., Sun, T., Wang, K., Luo, H., & Zhu, Y. (2022). Evaluating the Tsunamigenic potential of buried versus trench-breaching megathrust slip. *Journal of Geophysical Research: Solid Earth*, *127*(8), e2021JB023722. https://doi.org/10.1029/2021jb023722

Cera, T. B. (2011). Tidal analysis program in python (TAPPY). Software Repository. Retrieved from https://github.com/pwcazenave/tappy

Chaudhuri, K., & Ghosh, A. (2022). Widespread very low frequency earthquakes (VLFEs) activity offshore Cascadia. *Geophysical Research Letters*, *49*(13), e2022GL097962. https://doi.org/10.1029/2022gl097962

Davis, E. E., Becker, K., Kyo, M., & Kimura, T. (2018). Foundational experiences and recent advances in long-term deep-ocean borehole observatories for hydrologic, geodetic, and seismic monitoring. *Marine Technology Society Journal*, *52*(5), 74–86. https://doi.org/10.4031/mtsj.52.5.4

Davis, E. E., Becker, K., Wang, K., & Kinoshita, M. (2009). Co-seismic and post-seismic pore-fluid pressure changes in the Philippine Sea plate and Nankai decollement in response to a seismogenic strain event off Kii Peninsula, Japan. *Earth Planets and Space*, *61*(6), 649–657. https://doi.org/10.1186/bf03353174

Davis, E. E., & Farrugia, J. J. (2021). Amplification and tuning of ground motion at the outer Cascadia accretionary prism. *Journal of Geophysical Research: Solid Earth*, *126*(5), e2020JB020950. https://doi.org/10.1029/2020jb020950

Davis, E. E., & Heesemann, M. (2012). IODP expedition 328: Early results of Cascadia subduction zone ACORK observatory. *Scientific Drilling*, *13*, 12–18. https://doi.org/10.5194/sd-13-12-2012

Davis, E. E., & Hyndman, R. D. (1989). Accretion and recent deformation of sediments along the northern Cascadia subduction zone. *Geological Society of America Bulletin*, *101*(11), 1465–1480. https://doi.org/10.1130/0016-7606(1989)101<1465:aardos>2.3.co;2

Davis, E. E., Hyndman, R. D., & Villinger, H. (1990). Rates of fluid expulsion across the Northern Cascadia Accretionary Prism: Constraints from new heat row and multichannel seismic reflection data. *Journal of Geophysical Research*, *95*(B6), 8869–8889. https://doi.org/10.1029/jb095ib06p08869

Davis, E. E., Kinoshita, M., Becker, K., Wang, K., Asano, Y., & Ito, Y. (2013). Episodic deformation and inferred slow slip at the Nankai subduction zone during the first decade of CORK borehole pressure and VLFE monitoring. *Earth and Planetary Science Letters*, *368*, 110–118. https://doi.org/10.1016/j.epsl.2013.03.009

Davis, E. E., Malone, M. J., & The Expedition 328 Scientists and Engineers. (2010). Cascadia subduction zone ACORK observatory. In *Integrated Ocean Drilling Program Preliminary Report* (p. 328).

Davis, E. E., Villinger, H., & Sun, T. (2015). Slow and delayed deformation and uplift of the outermost subduction prism following ETS and seismogenic slip events beneath Nicoya Peninsula, Costa Rica. *Earth and Planetary Science Letters*, *410*, 117–127. https://doi.org/10.1016/j.epsl.2014.11.015

DeSanto, J. B., Schmidt, D. A., Chadwell, C. D., Zumberge, M. A., & Sasagawa, G. S. (2022). Horizontal deformation rates near the Cascadia subduction zone trench revealed by offshore GNSS-Acoustic time series. In *Abstract T56A-05 (Fall Meeting, AGU, Chicago, 12–16 December 2022)*. Retrieved from https://agu.confex.com/agu/fm22/meetingapp.cgi/Paper/1193941

Dragert, H., Wang, K., & James, T. S. (2001). A silent slip event on the deeper Cascadia subduction interface. *Science*, *292*(5521), 1525–1528. https://doi.org/10.1126/science.1060152

Dragert, H., Wang, K., & Rogers, G. (2004). Geodetic and seismic signatures of episodic tremor and slip in the northern Cascadia subduction zone. *Earth Planets and Space*, *56*(12), 1143–1150. https://doi.org/10.1186/bf03353333

Fredrickson, E. K., Wilcock, W. S., Schmidt, D. A., MacCready, P., Roland, E., Kurapov, A. L., et al. (2019). Optimizing sensor configurations for the detection of slow-slip earthquakes in seafloor pressure records, using the Cascadia subduction zone as a case study. *Journal of Geophysical Research: Solid Earth*, *124*(12), 13504–13531. https://doi.org/10.1029/2019jb018053

Gao, D., Wang, K., Insua, T. L., Sypus, M., Riedel, M., & Sun, T. (2018). Defining megathrust tsunami source scenarios for northernmost Cascadia. *Natural Hazards*, *94*(1), 445–469. https://doi.org/10.1007/s11069-018-3397-6

Goldfinger, C., Nelson, C. H., Morey, A. E., Johnson, J. E., Patton, J. R., Karabanov, E. B., et al. (2012). *Turbidite event history—Methods and implications for Holocene paleoseismicity of the Cascadia subduction zone (No. 1661-F)*. US Geological Survey.

Gomberg, J., Reasenberg, P. A., Bodin, P. L., & Harris, R. A. (2001). Earthquake triggering by seismic waves following the Landers and Hector Mine earthquakes. *Nature*, *411*(6836), 462–466. https://doi.org/10.1038/35078053

Gong, J., & McGuire, J. J. (2021). Constraints on the geometry of the subducted Gorda plate from converted phases generated by local earthquakes. *Journal of Geophysical Research: Solid Earth*, *126*(2), e2020JB019962. https://doi.org/10.1029/2020jb019962

Haacke, R. R., Westbrook, G. K., & Hyndman, R. D. (2007). Gas hydrate, fluid flow and free gas: Formation of the bottom-simulating reflector. *Earth and Planetary Science Letters*, *261*(3–4), 407–420. https://doi.org/10.1016/j.epsl.2007.07.008

Han, S., Bangs, N. L., Carbotte, S. M., Saffer, D. M., & Gibson, J. C. (2017). Links between sediment consolidation and Cascadia megathrust slip behaviour. *Nature Geoscience*, *10*(12), 954–959. https://doi.org/10.1038/s41561-017-0007-2

Han, S., Carbotte, S. M., Canales, J. P., Nedimović, M. R., Carton, H., Gibson, J. C., & Horning, G. W. (2016). Seismic reflection imaging of the Juan de Fuca plate from ridge to trench: New constraints on the distribution of faulting and evolution of the crust prior to subduction. *Journal of Geophysical Research: Solid Earth*, *121*(3), 1849–1872. https://doi.org/10.1002/2015jb012416

Hayes, G. P. (2017). The finite, kinematic rupture properties of great-sized earthquakes since 1990. *Earth and Planetary Science Letters*, *468*, 94–100. https://doi.org/10.1016/j.epsl.2017.04.003

Hayes, G. P., Moore, G. L., Portner, D. E., Hearne, M., Flamme, H., Furtney, M., & Smoczyk, G. M. (2018). Slab2, a comprehensive subduction zone geometry model. *Science*, *362*(6410), 58–61. https://doi.org/10.1126/science.aat4723

Heesemann, M., Insua, T. L., Scherwath, M., Juniper, K. S., & Moran, K. (2014). Ocean networks Canada: From geohazards research laboratories to smart ocean systems. *Oceanography*, *27*(2), 151–153. https://doi.org/10.5670/oceanog.2014.50

Hill, D. P. (2008). Dynamic stresses, Coulomb failure, and remote triggering. *Bulletin of the Seismological Society of America*, *98*(1), 66–92. https://doi.org/10.1785/0120070049

Hutchinson, J., & Heesemann, M. (2022). Initial results from the Northern Cascadia Subduction Zone Observatory (NCSZO). In *Abstract G34A-04 (Fall Meeting, AGU, Chicago, 12–16 December 2022)*. Retrieved from https://agu.confex.com/agu/fm22/meetingapp.cgi/Paper/1122360

Hutchinson, J., Kao, H., Riedel, M., Obana, K., Wang, K., Kodaira, S., et al. (2020). Significant geometric variation of the subducted plate beneath the northernmost Cascadia subduction zone and its tectonic implications as revealed by the 2014 M_w 6.4 earthquake sequence. *Earth and Planetary Science Letters*, *551*, 116569. https://doi.org/10.1016/j.epsl.2020.116569

Hutchinson, J., Kao, H., Spence, G., Obana, K., Wang, K., & Kodaira, S. (2019). Seismic characteristics of the Nootka Fault Zone: Results from the seafloor earthquake array Japan–Canada Cascadia experiment (SeaJade). *Bulletin of the Seismological Society of America*, *109*(6), 2252–2276. https://doi.org/10.1785/0120190008

Hyndman, R. D., & Davis, E. E. (1992). A mechanism for the formation of methane hydrate and seafloor bottom-simulating reflectors by vertical fluid expulsion. *Journal of Geophysical Research*, *97*(B5), 7025–7041. https://doi.org/10.1029/91jb03061

Hyndman, R. D., & Wang, K. (1993). Thermal constraints on the zone of major thrust earthquake failure: The Cascadia subduction zone. *Journal of Geophysical Research*, *98*(B2), 2039–2060. https://doi.org/10.1029/92jb02279

Hyndman, R. D., Yorath, C. J., Clowes, R. M., & Davis, E. E. (1990). The northern Cascadia subduction zone at Vancouver Island: Seismic structure and tectonic history. *Canadian Journal of Earth Sciences*, *27*(3), 313–329. https://doi.org/10.1139/e90-030

Ide, S., Beroza, G. C., Shelly, D. R., & Uchide, T. (2007). A scaling law for slow earthquakes. *Nature*, *447*(7140), 76–79. https://doi.org/10.1038/nature05780

Ikari, M. J., Saffer, D. M., & Marone, C. (2009). Frictional and hydrologic properties of clay-rich fault gouge. *Journal of Geophysical Research*, *114*(B5), B05409. https://doi.org/10.1029/2008jb006089

Inoue, T., Ito, Y., Wallace, L. M., Yoshikawa, Y., Inazu, D., Garcia, E. S. M., et al. (2021). Water depth dependence of long-range correlation in nontidal variations in seafloor pressure. *Geophysical Research Letters*, *48*(8), e2020GL092173. https://doi.org/10.1029/2020gl092173
International Seismological Centre. (2022). On-line bulletin. https://doi.org/10.31905/D808B830
Ito, Y., Hino, R., Kido, M., Fujimoto, H., Osada, Y., Inazu, D., et al. (2013). Episodic slow slip events in the Japan subduction zone before the 2011 Tohoku-Oki earthquake. *Tectonophysics*, *600*, 14–26. https://doi.org/10.1016/j.tecto.2012.08.022
Kido, M., Osada, Y., Fujimoto, H., Hino, R., & Ito, Y. (2011). Trench-normal variation in observed seafloor displacements associated with the 2011 Tohoku-Oki earthquake. *Geophysical Research Letters*, *38*(24), L24303. https://doi.org/10.1029/2011gl050057
Langer, L., Beller, S., Hirakawa, E., & Tromp, J. (2023). Impact of sedimentary basins on Green's functions for static slip inversion. *Geophysical Journal International*, *232*(1), 569–580. https://doi.org/10.1093/gji/ggac344
Lay, T. (2015). The surge of great earthquakes from 2004 to 2014. *Earth and Planetary Science Letters*, *409*, 133–146. https://doi.org/10.1016/j.epsl.2014.10.047
Li, S., Wang, K., Wang, Y., Jiang, Y., & Dosso, S. E. (2018). Geodetically inferred locking state of the Cascadia megathrust based on a viscoelastic Earth model. *Journal of Geophysical Research: Solid Earth*, *123*(9), 8056–8072. https://doi.org/10.1029/2018jb015620
Lindsey, E. O., Mallick, R., Hubbard, J. A., Bradley, K. E., Almeida, R. V., Moore, J. D., et al. (2021). Slip rate deficit and earthquake potential on shallow megathrusts. *Nature Geoscience*, *14*(5), 321–326. https://doi.org/10.1038/s41561-021-00736-x
McCaffrey, R., King, R. W., Payne, S. J., & Lancaster, M. (2013). Active tectonics of northwestern US inferred from GPS-derived surface velocities. *Journal of Geophysical Research: Solid Earth*, *118*(2), 709–723. https://doi.org/10.1029/2012jb009473
McCrory, P. A., Blair, J. L., Oppenheimer, D. H., & Walter, S. R. (2004). Depth to the Juan de Fuca slab beneath the Cascadia subduction margin—A 3-D model for sorting earthquakes. In *U.S. Geological Survey Date Series 91*. https://doi.org/10.3133/ds91
McCrory, P. A., Blair, J. L., Waldhauser, F., & Oppenheimer, D. H. (2012). Juan de Fuca slab geometry and its relation to Wadati-Benioff zone seismicity. *Journal of Geophysical Research*, *117*(B9), B09306. https://doi.org/10.1029/2012jb009407
McGuire, J. J., Collins, J. A., Davis, E., Becker, K., & Heesemann, M. (2018). A lack of dynamic triggering of slow slip and tremor indicates that the shallow Cascadia megathrust offshore Vancouver Island is likely locked. *Geophysical Research Letters*, *45*(20), 11-095. https://doi.org/10.1029/2018gl079519
Melgar, D., Sahakian, V. J., & Thomas, A. M. (2022). Deep coseismic slip in the Cascadia megathrust can be consistent with coastal subsidence. *Geophysical Research Letters*, *49*(3), e2021GL097404. https://doi.org/10.1029/2021gl097404
Morton, E. A., Bilek, S. L., & Rowe, C. A. (2018). Newly detected earthquakes in the Cascadia subduction zone linked to seamount subduction and deformed upper plate. *Geology*, *46*(11), 943–946. https://doi.org/10.1130/g45354.1
Nedimović, M. R., Hyndman, R. D., Ramachandran, K., & Spence, G. D. (2003). Reflection signature of seismic and aseismic slip on the northern Cascadia subduction interface. *Nature*, *424*(6947), 416–420. https://doi.org/10.1038/nature01840
Obara, K., & Kato, A. (2016). Connecting slow earthquakes to huge earthquakes. *Science*, *353*(6296), 253–257. https://doi.org/10.1126/science.aaf1512
Okada, Y. (1992). Internal deformation due to shear and tensile faults in a half-space. *Bulletin of the Seismological Society of America*, *82*(2), 1018–1040. https://doi.org/10.1785/bssa0820021018
Peng, Z., & Gomberg, J. (2010). An integrated perspective of the continuum between earthquakes and slow-slip phenomena. *Nature Geoscience*, *3*(9), 599–607. https://doi.org/10.1038/ngeo940
Pollitz, F. F., & Evans, E. L. (2017). Implications of the earthquake cycle for inferring fault locking on the Cascadia megathrust. *Geophysical Journal International*, *209*(1), 167–185. https://doi.org/10.1093/gji/ggx009
Prada, M., Galvez, P., Ampuero, J. P., Sallares, V., Sánchez-Linares, C., Macías, J., & Peter, D. (2021). The influence of depth-varying elastic properties of the upper plate on megathrust earthquake rupture dynamics and tsunamigenesis. *Journal of Geophysical Research: Solid Earth*, *126*(11), e2021JB022328. https://doi.org/10.1029/2021jb022328
Priest, G. R., Goldfinger, C., Wang, K., Witter, R. C., Zhang, Y., & Baptista, A. M. (2010). Confidence levels for tsunami-inundation limits in northern Oregon inferred from a 10,000-year history of great earthquakes at the Cascadia subduction zone. *Natural Hazards*, *54*(1), 27–73. https://doi.org/10.1007/s11069-009-9453-5
Riedel, M., Tréhu, A. M., & Spence, G. D. (2010). Characterizing the thermal regime of cold vents at the northern Cascadia margin from bottom-simulating reflector distributions, heat-probe measurements and borehole temperature data. *Marine Geophysical Researches*, *31*(1–2), 1–16. https://doi.org/10.1007/s11001-010-9080-2
Riedel, M., Willoughby, E. C., Chen, M. A., He, T., Novosel, I., Schwalenberg, K., et al. (2006). Gas hydrate on the northern Cascadia margin: Regional geophysics and structural framework. In *Proceedings of the Integrated Ocean Drilling program* (Vol. 311). Texas A & M University.
Rogers, G., & Dragert, H. (2003). Episodic tremor and slip on the Cascadia subduction zone: The chatter of silent slip. *Science*, *300*(5627), 1942–1943. https://doi.org/10.1126/science.1084783
Saffer, D. M., & Tobin, H. J. (2011). Hydrogeology and mechanics of subduction zone forearcs: Fluid flow and pore pressure. *Annual Review of Earth and Planetary Sciences*, *39*(1), 157–186. https://doi.org/10.1146/annurev-earth-040610-133408
Saffer, D. M., & Wallace, L. M. (2015). The frictional, hydrologic, metamorphic and thermal habitat of shallow slow earthquakes. *Nature Geoscience*, *8*(8), 594–600. https://doi.org/10.1038/ngeo2490
Sallarès, V., & Ranero, C. R. (2019). Upper-plate rigidity determines depth-varying rupture behaviour of megathrust earthquakes. *Nature*, *576*(7785), 96–101. https://doi.org/10.1038/s41586-019-1784-0
Sato, M., Ishikawa, T., Ujihara, N., Yoshida, S., Fujita, M., Mochizuki, M., & Asada, A. (2011). Displacement above the hypocenter of the 2011 Tohoku-Oki earthquake. *Science*, *332*(6036), 1395. https://doi.org/10.1126/science.1207401
Saux, J. P., Molitors Bergman, E. G., Evans, E. L., & Loveless, J. P. (2022). The role of slow slip events in the Cascadia subduction zone earthquake cycle. *Journal of Geophysical Research: Solid Earth*, *127*(2), e2021JB022425. https://doi.org/10.1029/2021jb022425
Schmalzle, G. M., McCaffrey, R., & Creager, K. C. (2014). Central Cascadia subduction zone creep. *Geochemistry, Geophysics, Geosystems*, *15*(4), 1515–1532. https://doi.org/10.1002/2013gc005172
Scholz, C. H. (1998). Earthquakes and friction laws. *Nature*, *391*(6662), 37–42. https://doi.org/10.1038/34097
Stanislowski, K., Roesner, A., & Ikari, M. J. (2022). Implications for megathrust slip behavior and pore pressure at the shallow northern Cascadia subduction zone from laboratory friction experiments. *Earth and Planetary Science Letters*, *578*, 117297. https://doi.org/10.1016/j.epsl.2021.117297
Stone, I., Vidale, J. E., Han, S., & Roland, E. (2018). Catalog of offshore seismicity in Cascadia: Insights into the regional distribution of microseismicity and its relation to subduction processes. *Journal of Geophysical Research: Solid Earth*, *123*(1), 641–652. https://doi.org/10.1002/2017jb014966

Sun, T., & Davis, E. E. (2022). Monitoring the 2021 M_w 8.2 Alaska earthquake by an offshore seismic and fluid pressure observation network and implications for ocean-crust dynamic coupling. *Geochemistry, Geophysics, Geosystems*, *23*(9), e2022GC010540. https://doi.org/10.1029/2022gc010540

Sun, T., Davis, E. E., & Heesemann, M. (2021). Seismic formation fluid pressure observations reveal high anisotropy of oceanic crust. *Geophysical Research Letters*, *48*(20), e2021GL095347. https://doi.org/10.1029/2021gl095347

Sun, T., Davis, E. E., Wang, K., & Jiang, Y. (2017). Trench-breaching afterslip following deeper coseismic slip of the 2012 M_w 7.6 Costa Rica earthquake constrained by near-trench pressure and land-based geodetic observations. *Earth and Planetary Science Letters*, *479*, 263–272. https://doi.org/10.1016/j.epsl.2017.09.021

Sun, T., Ellis, S., & Saffer, D. (2020). Coupled evolution of deformation, pore fluid pressure, and fluid flow in shallow subduction forearcs. *Journal of Geophysical Research: Solid Earth*, *125*(3), e2019JB019101. https://doi.org/10.1029/2019jb019101

Sun, T., Wang, K., Fujiwara, T., Kodaira, S., & He, J. (2017). Large fault slip peaking at trench in the 2011 Tohoku-oki earthquake. *Nature Communications*, *8*(1), 14044. https://doi.org/10.1038/ncomms14044

Sun, T., Wang, K., Iinuma, T., Hino, R., He, J., Fujimoto, H., et al. (2014). Prevalence of viscoelastic relaxation after the 2011 Tohoku-oki earthquake. *Nature*, *514*(7520), 84–87. https://doi.org/10.1038/nature13778

Tobin, H. J. (2022). Re-examining the prospects for frictional locking and seismic slip of the Cascadia shallow megathrust and accretionary wedge faults. In *Abstract T53B-05 (Fall Meeting, AGU, Chicago, 12–16 December 2022)*. Retrieved from https://agu.confex.com/agu/fm22/meetingapp.cgi/Paper/1187315

Tomita, F., Kido, M., Ohta, Y., Iinuma, T., & Hino, R. (2017). Along-trench variation in seafloor displacements after the 2011 Tohoku earthquake. *Science Advances*, *3*(7), e1700113. https://doi.org/10.1126/sciadv.1700113

Toomey, D. R., Allen, R. M., Barclay, A. H., Bell, S. W., Bromirski, P. D., Carlson, R. L., et al. (2014). The Cascadia initiative: A sea change in seismological studies of subduction zones. *Oceanography*, *27*(2), 138–150. https://doi.org/10.5670/oceanog.2014.49

Tréhu, A. M., Blakely, R. J., & Williams, M. C. (2012). Subducted seamounts and recent earthquakes beneath the central Cascadia forearc. *Geology*, *40*(2), 103–106. https://doi.org/10.1130/g32460.1

Tréhu, A. M., Braunmiller, J., & Davis, E. (2015). Seismicity of the central Cascadia continental margin near 44.5N: A decadal view. *Seismological Research Letters*, *86*(3), 819–829. https://doi.org/10.1785/0220140207

Ulrich, T., Gabriel, A. A., & Madden, E. H. (2022). Stress, rigidity and sediment strength control megathrust earthquake and tsunami dynamics. *Nature Geoscience*, *15*(1), 67–73. https://doi.org/10.1038/s41561-021-00863-5

van Der Elst, N. J., & Brodsky, E. E. (2010). Connecting near-field and far-field earthquake triggering to dynamic strain. *Journal of Geophysical Research*, *115*(B7), B07311. https://doi.org/10.1029/2009jb006681

Wallace, L. M. (2020). Slow slip events in New Zealand. *Annual Review of Earth and Planetary Sciences*, *48*(1), 175–203. https://doi.org/10.1146/annurev-earth-071719-055104

Wallace, L. M., Araki, E., Saffer, D., Wang, X., Roesner, A., Kopf, A., et al. (2016). Near-field observations of an offshore M_w 6.0 earthquake from an integrated seafloor and subseafloor monitoring network at the Nankai Trough, southwest Japan. *Journal of Geophysical Research: Solid Earth*, *121*(11), 8338–8351. https://doi.org/10.1002/2016jb013417

Wallace, L. M., Kaneko, Y., Hreinsdóttir, S., Hamling, I., Peng, Z., Bartlow, N., et al. (2017). Large-scale dynamic triggering of shallow slow slip enhanced by overlying sedimentary wedge. *Nature Geoscience*, *10*(10), 765–770. https://doi.org/10.1038/ngeo3021

Wallace, L. M., Saffer, D., Davis, E., Williams, C., & Woods, K. (2021). Near-field observations of shallow slow slip events revealed by IODP observatories at the Hikurangi subduction zone. In *Abstract T21A-08 (Fall Meeting, AGU, New Orleans, 13–17 December 2021)*. Retrieved from https://ui.adsabs.harvard.edu/abs/2021AGUFM.T21A..08W/abstract

Wallace, L. M., Webb, S. C., Ito, Y., Mochizuki, K., Hino, R., Henrys, S., et al. (2016). Slow slip near the trench at the Hikurangi subduction zone, New Zealand. *Science*, *352*(6286), 701–704. https://doi.org/10.1126/science.aaf2349

Walton, M. A., Staisch, L. M., Dura, T., Pearl, J. K., Sherrod, B., Gomberg, J., et al. (2021). Toward an integrative geological and geophysical view of Cascadia subduction zone earthquakes. *Annual Review of Earth and Planetary Sciences*, *49*(1), 367–398. https://doi.org/10.1146/annurev-earth-071620-065605

Wang, K., & Davis, E. E. (1996). Theory for the propagation of tidally induced pore pressure variations in layered subseafloor formations. *Journal of Geophysical Research*, *101*(B5), 11483–11495. https://doi.org/10.1029/96jb00641

Wang, K., Davis, E. E., & van der Kamp, G. (1998). Theory for the effects of free gas in subsea formations on tidal pore pressure variations and seafloor displacements. *Journal of Geophysical Research*, *103*(B6), 12339–12353. https://doi.org/10.1029/98jb00952

Wang, K., & Dixon, T. (2004). "Coupling" semantics and science in earthquake research. *Eos, Transactions American Geophysical Union*, *85*(18), 180. https://doi.org/10.1029/2004eo180005

Wang, K., Sun, T., Brown, L., Hino, R., Tomita, F., Kido, M., et al. (2018). Learning from crustal deformation associated with the M9 2011 Tohoku-oki earthquake. *Geosphere*, *14*(2), 552–571. https://doi.org/10.1130/ges01531.1

Wang, K., & Tréhu, A. M. (2016). Invited review paper: Some outstanding issues in the study of great megathrust earthquakes—The Cascadia example. *Journal of Geodynamics*, *98*, 1–18. https://doi.org/10.1016/j.jog.2016.03.010

Wang, K., Wells, R., Mazzotti, S., Hyndman, R. D., & Sagiya, T. (2003). A revised dislocation model of interseismic deformation of the Cascadia subduction zone. *Journal of Geophysical Research*, *108*(B1), 2026. https://doi.org/10.1029/2001jb001227

Wang, P. L., Engelhart, S. E., Wang, K., Hawkes, A. D., Horton, B. P., Nelson, A. R., & Witter, R. C. (2013). Heterogeneous rupture in the great Cascadia earthquake of 1700 inferred from coastal subsidence estimates. *Journal of Geophysical Research: Solid Earth*, *118*(5), 2460–2473. https://doi.org/10.1002/jgrb.50101

Watanabe, S. I., Sato, M., Fujita, M., Ishikawa, T., Yokota, Y., Ujihara, N., & Asada, A. (2014). Evidence of viscoelastic deformation following the 2011 Tohoku-Oki earthquake revealed from seafloor geodetic observation. *Geophysical Research Letters*, *41*(16), 5789–5796. https://doi.org/10.1002/2014gl061134

Westbrook, G. K., Carson, B., & Musgrave, R. J. (1994). Leg 146. Introduction: Cascadia margin. In *Proceedings of the ODP initial report* (Vol. 146, pp. 5–14).

Wilcock, W. S., Manalang, D. A., Fredrickson, E. K., Harrington, M. J., Cram, G., Tilley, J., et al. (2021). A thirty-month seafloor test of the A-0-A method for calibrating pressure gauges. *Frontiers of Earth Science*, *8*, 600671. https://doi.org/10.3389/feart.2020.600671

Williams, C. A., & Wallace, L. M. (2018). The impact of realistic elastic properties on inversions of shallow subduction interface slow slip events using seafloor geodetic data. *Geophysical Research Letters*, *45*(15), 7462–7470. https://doi.org/10.1029/2018gl078042

Woods, K., Webb, S. C., Wallace, L. M., Ito, Y., Collins, C., Palmer, N., et al. (2022). Using seafloor geodesy to detect vertical deformation at the Hikurangi subduction zone: Insights from self-calibrating pressure sensors and ocean general circulation models. *Journal of Geophysical Research: Solid Earth*, *127*(12), e2022JB023989. https://doi.org/10.1029/2022jb023989

Yokota, Y., Ishikawa, T., Watanabe, S. I., Tashiro, T., & Asada, A. (2016). Seafloor geodetic constraints on interplate coupling of the Nankai Trough megathrust zone. *Nature*, *534*(7607), 374–377. https://doi.org/10.1038/nature17632

Yuan, T., Spence, G. D., & Hyndman, R. D. (1994). Seismic velocities and inferred porosities in the accretionary wedge sediments at the Cascadia margin. *Journal of Geophysical Research*, *99*(B3), 4413–4427. https://doi.org/10.1029/93jb03203